International Journal of
Thermofluid Science and Technology

MDPI

Article

Physics-Informed Modeling of Transient Pulsating Microchannel Flow with Heat-Transfer and Entropy-Generation Trade-Off Analysis

Aswin Karkadakattil

Independent Researcher, Kasaragod 671313, India; ashwinharik20000@gmail.com

Abstract

Pulsating flow offers a practical means of modifying convective heat transfer in microchannels, but thermal enhancement may be accompanied by increased thermodynamic irreversibility. This study develops a physics-informed neural network (PINN) framework that couples transient thermo-fluid prediction with concurrent heat-transfer and entropy-generation assessment, rather than considering heat transfer alone. The continuity, momentum, and energy equations are embedded directly into the training process, with residual-based adaptive refinement used to improve solution resolution in high-residual regions. Independent verification of the steady reference solution gives relative discrepancies of 0.04% for the velocity profile against the analytical fully developed parabolic reference, 0.08% for the temperature profile against the finite-difference benchmark, and 3.51% for the downstream Nusselt number against the finite-difference benchmark. For the representative pulsating condition, the phase-resolved Nusselt number decreases from 5.0435 to 4.5413 (9.96%), while total entropy generation increases by 11.16% over the examined phases. The completed 27-case parameter sweep reveals a non-monotonic dependence on pulsation amplitude and frequency, indicating that stronger pulsation does not necessarily produce greater heat-transfer enhancement. Within the investigated parameter space, the condition $A = 0.2, f = 20$ Hz, and $\phi_1 = \phi_2 = 0.015$ gives the highest mean Nusselt number of 7.1126, together with the lowest total entropy generation of 2.7496×10^{-4} W/K among the evaluated cases. These results demonstrate a physics-constrained framework for jointly evaluating thermal performance and thermodynamic cost, providing a more comprehensive basis for assessing pulsation conditions than heat-transfer enhancement alone.

Keywords: physics-informed neural network (PINN); pulsating microchannel flow; convective heat transfer; Nusselt number; entropy generation; thermodynamic irreversibility; residual-based adaptive refinement; transient thermo-fluid analysis; pareto analysis

Check for updates

Academic Editor: Xiande Fang

Received: 30 August 2026
Revised: 1 October 2026
Accepted: 20 October 2026
Published: 28 October 2026

Copyright: © 2026 by the author. Published by MDPI on behalf of the Nanjing University of Aeronautics and Astronautics. Licensee MDPI, Basel, Switzerland. This article is an open access article distributed under the terms and conditions of the Creative Commons Attribution (CC BY) license.

1. Introduction

1.1. Pulsating Flow as a Thermal-Management Strategy

The continued miniaturization of electronic and thermal systems has increased the demand for cooling technologies capable of removing high heat loads from increasingly confined spaces. Microchannels are particularly attractive for this purpose because their small hydraulic dimensions provide a high surface-to-volume ratio, promoting effective interaction between the coolant and heated surfaces. Consequently, microchannel heat sinks have become an important option for thermal-management applications subject to

tight geometric and power constraints [1–12]. Research on microchannel cooling has addressed fundamental issues in flow boiling [4], single-phase frictional pressure losses [6], numerical heat-transfer prediction [7], and the influence of nanofluid properties on cooling performance [8], alongside experimental and numerical investigations of pressure drop and heat transfer [5]. However, improving heat removal is not simply a matter of increasing the flow rate. Higher flow rates can increase hydraulic resistance and pumping requirements, while persistent hydrodynamic and thermal boundary layers can limit convective transport [2,3,6,9–12]. Pulsating flow offers an alternative by periodically varying the inlet velocity, thereby modifying the local momentum and thermal fields. This unsteadiness can disturb developing boundary layers, redistribute momentum, and alter temperature distributions, influencing the convective heat-transfer coefficient and Nusselt number [13–19]. Recent investigations have examined pulsating-flow configurations and the effects of oscillation frequency and amplitude on heat-transfer performance [14,18,19]. These parameters govern the magnitude and timescale of the imposed disturbance and interact with the developing flow and thermal fields to determine the resulting thermal response [19]. Nevertheless, enhanced heat transfer does not necessarily translate into better overall thermal performance. Stronger flow disturbances may increase velocity and temperature gradients, affecting viscous dissipation, heat-transfer irreversibility, and total entropy generation [20–26]. Therefore, pulsating flow should be assessed by considering heat-transfer enhancement alongside its thermodynamic cost. This motivates an integrated evaluation of thermal transport and irreversibility to identify operating conditions that provide an appropriate balance between heat-transfer performance and entropy generation.

1.2. Heat-Transfer Enhancement Versus Thermodynamic Cost

The Nusselt number is a standard measure of convective heat-transfer performance and is widely used to compare different microchannel operating conditions [2,5]. A higher Nusselt number generally indicates stronger convective transport relative to conduction. For this reason, many thermal-management studies naturally use the Nusselt number as a primary indicator of the effectiveness of flow modifications. For pulsating microchannel flow, however, this quantity alone does not provide a complete picture. Heat transfer occurs simultaneously with irreversible processes. Temperature gradients contribute to thermal entropy generation, while velocity gradients contribute to viscous irreversibility [20–26]. Under pulsating conditions, both types of gradients can change with the instantaneous flow state. Consequently, changing the pulsation amplitude or frequency may improve heat transfer while also altering the thermodynamic cost associated with maintaining that transport.

Entropy generation provides a complementary measure of this behavior. The entropy-generation framework introduced by Bejan provides a thermodynamic basis for quantifying the irreversibility associated with heat and fluid transport [21–23]. Its application to microchannel systems has subsequently been used to examine the relationship between thermal performance and irreversible losses [24–26]. For pulsating systems, this perspective is particularly relevant because unsteady flow can modify both the thermal gradients associated with heat transfer and the velocity gradients responsible for viscous losses [20]. The engineering question therefore extends beyond simply identifying which operating condition produces the largest Nusselt number. It also involves determining which conditions provide useful thermal enhancement without imposing an unnecessarily large thermodynamic penalty. This distinction is central to the present study. Entropy generation is therefore considered alongside the Nusselt number when evaluating the investigated operating conditions. This combined perspective is particularly relevant at the microscale, where small characteristic dimensions can produce strong spatial gradients and where

changes in operating conditions may alter the balance between convective transport and irreversible losses.

1.3. Computational Challenge of Transient Parameter Exploration

Although pulsation provides an additional degree of control over microchannel transport, systematic exploration of its operating parameters is computationally demanding. Even a relatively modest investigation requires the effects of amplitude and frequency to be considered together. When different nanoparticle-loading conditions are also considered, each combination can produce a different transient thermo-fluid response that must be resolved before meaningful heat-transfer and entropy-generation measures can be obtained. Conventional numerical methods remain essential tools for this type of problem and provide an important basis for independent benchmarking. However, repeatedly solving transient problems for multiple operating conditions can become computationally intensive, particularly when the objective is to map an operating space rather than obtain a single flow solution. Physics-informed neural networks (PINNs) provide an equation-constrained framework that can be used for such problems. Rather than relying exclusively on a database of precomputed solutions, PINNs incorporate the governing differential equations and boundary conditions directly into the training process [27–30]. The neural network therefore represents the thermo-fluid fields while being constrained by the physical equations governing their behavior. This makes PINNs attractive for coupled transport problems in which transient flow and temperature fields must be resolved under different operating conditions. Importantly, the use of a PINN does not by itself guarantee engineering accuracy or computational superiority over conventional CFD or finite-difference methods. PINN performance depends on the mathematical formulation, collocation strategy, optimization procedure, and treatment of physical constraints [27–30]. This consideration is particularly important when derived quantities such as the Nusselt number and entropy generation are calculated from spatial gradients. A visually smooth solution is therefore not sufficient evidence of quantitative accuracy. Independent verification is an important part of establishing confidence in the predicted thermo-fluid fields and their derived quantities. For this reason, the present study adopts a validation-first strategy. The steady PINN formulation is first compared with an independent finite-difference benchmark, and the resulting agreement is used to establish a quantitative reference before the framework is applied to the transient pulsating-flow analysis and subsequent parameter screening.

1.4. Limitations of Existing Approaches

Previous research provides a strong foundation for microchannel heat transfer, pulsating-flow enhancement, entropy-generation analysis, and physics-informed computational methods. Nevertheless, these areas have largely developed along separate methodological paths.

First, many microchannel studies primarily evaluate thermal performance using quantities such as heat-transfer coefficient, Nusselt number, pressure drop, or temperature reduction [2,5,9–12]. These metrics are essential for characterizing cooling performance, but heat-transfer enhancement alone does not indicate whether an improvement is accompanied by an acceptable thermodynamic cost.

Second, pulsating-flow studies have demonstrated that amplitude and frequency can strongly influence heat transfer [15–19]. However, the transient nature of the problem means that the response cannot generally be inferred from a single steady calculation. Systematic exploration of multiple pulsation conditions therefore requires repeated resolution of the evolving flow and temperature fields.

Third, PINNs have developed rapidly as physics-constrained approaches for solving fluid and transport problems [27–30]. However, reproducing a physical field is not equivalent to demonstrating that a PINN can support quantitative engineering analysis. This distinction is particularly important when derived quantities are considered. The Nusselt number depends on wall heat transfer and thermal gradients, while entropy-generation calculations depend on gradients within the thermo-fluid field. Errors in the primary fields can therefore propagate into the derived engineering metrics.

Finally, heat-transfer and thermodynamic objectives are not always integrated into a single parameter-screening framework. Considering these quantities separately can obscure the trade-off between thermal enhancement and irreversibility. The operating condition associated with a high Nusselt number may not simultaneously minimize entropy generation.

These observations define the methodological gap addressed in the present work. The aim is not simply to apply another PINN to a pulsating-flow problem, but to develop a validated computational workflow that connects transient pulsating transport with quantitative heat-transfer and entropy-generation assessment and then uses both responses to identify non-dominated operating conditions. The present study is structured around this connection.

1.5. Research Objective and Contributions

The objective of this work is to develop and quantitatively assess a physics-informed framework for transient thermo-fluid transport in a pulsating microchannel and to use the framework to examine the coupled relationship between heat-transfer performance and thermodynamic irreversibility.

Four contributions are considered.

First, a physics-informed transient thermo-fluid framework is developed. The PINN represents the coupled flow and temperature fields under pulsating inlet conditions, while residual-based adaptive refinement is used to increase resolution in regions where the governing-equation residual is comparatively high. This provides a physics-constrained representation of the transient transport problem rather than a purely data-fitted approximation.

Second, the steady formulation is independently validated before parameter exploration. Comparison with an independent finite-difference benchmark gives relative differences of 0.04% for the velocity profile and 0.08% for the temperature profile. The downstream Nusselt number is 2.9969 from the PINN compared with 2.8953 from the finite-difference benchmark, corresponding to a 3.51% relative difference. This provides a quantitative reference for the subsequent transient analysis.

Third, heat-transfer and thermodynamic responses are evaluated together. The framework is used to examine how pulsation amplitude and frequency affect the Nusselt number and total entropy generation. This makes it possible to assess thermal enhancement together with the associated thermodynamic penalty rather than considering heat transfer in isolation.

Fourth, the two responses are combined through Pareto analysis. Instead of treating the highest Nusselt number as the sole criterion, the investigated operating points are evaluated according to their simultaneous heat-transfer and entropy-generation performance. The resulting non-dominated points provide a basis for examining the trade-off between thermal enhancement and thermodynamic irreversibility within the investigated parameter space. The central novelty of the study is therefore not the use of a PINN by itself. PINNs have already been established as physics-informed computational tools [27–30]. The novelty lies in their integration into a validation-first, thermodynamics-aware parameter-screening framework for pulsating microchannel flow. Independent quantitative validation is first used to establish confidence in the steady thermo-fluid solution; the framework is

then extended to transient pulsation analysis, and the resulting heat-transfer and entropy-generation responses are jointly examined to identify non-dominated operating conditions. In this way, the PINN is used as part of a broader physics-consistent framework linking transient transport, heat-transfer performance, thermodynamic irreversibility, and multi-objective operating-condition analysis.

2. Problem Formulation and Physics-Informed Methodology

2.1. Physical Configuration and Assumptions

A two-dimensional microchannel is considered to examine the effect of pulsating flow on convective heat transfer and the associated thermodynamic irreversibility. The channel has a length of $L = 2.0 \times 10^{-3}$ m and a height of $H = 2.0 \times 10^{-4}$ m, giving an aspect ratio of $H/L = 0.10$. The streamwise and transverse coordinates are denoted by x and y, respectively, with $0 \le x \le L$ and $0 \le y \le H$. The reference inlet velocity is $U_0 = 0.05$ m/s, and a uniform heat flux of $q'' = 2.0 \times 10^4$ W/m^2 is imposed at the lower wall. The reference temperature is $T_{\text{ref}} = 300$ K. These dimensional parameters are taken directly from the computational implementation. The transient inlet condition is prescribed as a periodically modulated fully developed plane-channel velocity profile. The implementation uses L as the common spatial scaling length, such that

$$X = \frac{x}{L}, Y = \frac{y}{L},$$

and the dimensionless channel height is therefore

$$H^* = \frac{H}{L} = 0.10.$$

The dimensionless time is defined as

$$\tau = \frac{tU_0}{L}.$$

With

$$\eta = \frac{Y}{H^*} = \frac{y}{H},$$

the implemented inlet velocity is

$$U_{\text{in}}(Y, \tau) = 6\eta(1 - \eta)[1 + A\sin(2\pi St\ \tau)],$$

where A is the pulsation amplitude and

$$St = \frac{fL}{U_0}$$

is the Strouhal number based on the channel length. The factor $6\eta(1 - \eta)$ represents a fully developed plane-Poiseuille profile with unit cross-sectional mean velocity. Importantly, no additional inlet phase parameter is used in the implemented boundary condition. Thus, A controls the strength of pulsation, whereas f controls its temporal frequency. When $A = 0$, the imposed inlet profile reduces to the steady parabolic profile and is physically independent of f. The different $A = 0$ cases in the numerical parameter sweep are therefore treated as separate numerical realizations of the same non-pulsating reference condition rather than as physically different frequency-dependent cases.

The channel walls satisfy the no-slip condition,

$$u = v = 0.$$

At the lower heated wall,

$$-k\frac{\partial T}{\partial y} = q'',$$

where k is the effective thermal conductivity of the hybrid nanofluid. With the temperature scaling

$$\theta = \frac{T - T_{\text{ref}}}{q'' L/k},$$

and the common coordinate scaling $Y = y/L$, the implemented dimensionless heat-flux condition becomes

$$\frac{\partial \theta}{\partial Y} = -1.$$

The upper wall is adiabatic,

$$\frac{\partial T}{\partial y} = 0,$$

and the outlet is imposed using a pressure-gauge condition together with zero streamwise gradients of velocity and temperature,

$$p = 0, \frac{\partial u}{\partial x} = 0, \frac{\partial v}{\partial x} = 0, \frac{\partial T}{\partial x} = 0.$$

For transient calculations, the initial condition is imposed at $\tau = 0$ using the unmodulated inlet profile ($A = 0$), with zero transverse velocity and the reference inlet temperature. These inlet, wall, outlet, and initial conditions are incorporated explicitly into the PINN objective.

The working fluid is a water-based hybrid nanofluid containing Al_2O_3 and Cu nanoparticles. The base-fluid properties used in the implementation are

$$\rho_f = 997.1 \text{ kg/m}^3,$$

$$c_{p,f} = 4179 \text{ J/(kg K)},$$

$$k_f = 0.613 \text{ W/(m K)},$$

And

$$\mu_f = 8.9 \times 10^{-4} \text{ Pa s}.$$

The corresponding nanoparticle properties are

$$\rho_{p1} = 3970 \text{ kg/m}^3, c_{p1} = 765 \text{ J/(kg K)}, k_{p1} = 40 \text{ W/(m K)}$$

for Al_2O_3, and

$$\rho_{p2} = 8933 \text{ kg/m}^3, c_{p2} = 385 \text{ J/(kg K)}, k_{p2} = 400 \text{ W/(m K)}$$

for Cu.

The nanoparticle volume fractions are denoted by

$$\phi_1 = \phi_{Al_2O_3}, \phi_2 = \phi_{Cu},$$

with the total nanoparticle concentration defined as

$$\phi = \phi_1 + \phi_2.$$

The computational study uses the paired concentration conditions

$$(\phi_1, \phi_2) = (0.005, 0.005), (0.010, 0.010), (0.015, 0.015).$$

Thus, ϕ_1 and ϕ_2 represent nanoparticle volume fractions and not pulsation phases. They are varied through the prescribed paired concentration levels rather than independently. This distinction is maintained throughout the manuscript.

For $\phi > 0$, the effective density is calculated from

$$\rho = (1-\phi)\rho_f + \phi_1\rho_{p1} + \phi_2\rho_{p2},$$

while the effective specific heat is evaluated from

$$c_p = \frac{(1-\phi)\rho_f c_{p,f} + \phi_1\rho_{p1}c_{p1} + \phi_2\rho_{p2}c_{p2}}{\rho}.$$

For zero nanoparticle loading, the implementation directly returns the base-fluid properties.

The effective thermal conductivity follows the Maxwell-type hybrid-mixture relation implemented in the code. Defining

$$k_{p,m} = \frac{\phi_1 k_{p1} + \phi_2 k_{p2}}{\phi},$$

the effective conductivity is

$$k = k_f \frac{k_{p,m} + 2k_f + 2\left(\phi_1 k_{p1} + \phi_2 k_{p2}\right) - 2\phi k_f}{k_{p,m} + 2k_f - \left(\phi_1 k_{p1} + \phi_2 k_{p2}\right) + \phi k_f}.$$

The effective dynamic viscosity is calculated using the Brinkman relation,

$$\mu = \frac{\mu_f}{(1-\phi)^{2.5}}.$$

The corresponding thermal diffusivity and kinematic viscosity are then obtained from

$$\alpha = \frac{k}{\rho c_p}, \nu = \frac{\mu}{\rho}.$$

These effective properties are recalculated for each prescribed (ϕ_1, ϕ_2) condition before the corresponding PINN problem is solved. The flow is assumed to be incompressible, single-phase, and laminar, with the effective-property description used to represent the hybrid nanofluid. The thermo-fluid solution is represented continuously by a neural network rather than by nodal values on a conventional computational mesh. The network receives the normalized spatial and temporal coordinates,

$$z = [X, Y, \tau],$$

and predicts the four field variables,

$$q = [U, V, P, \Theta],$$

where U, V, P, and Θ denote the dimensionless streamwise velocity, transverse velocity, pressure, and temperature, respectively. The implemented network contains three input variables, five hidden layers with 128 neurons per layer, and four output variables. Hyperbolic-tangent activation functions are used in the hidden layers, and the trainable weights are initialized using Xavier initialization. The PINN formulation enables the transient velocity and temperature fields to be obtained from the same physics-constrained representation, from which the local and spatially averaged heat-transfer quantities and entropy-generation measures are subsequently evaluated. Automatic differentiation is used to obtain the derivatives required by the governing residuals. The computational workflow first establishes the physical and dimensionless formulation, embeds the governing equations and boundary conditions into the PINN, and applies residual-based adaptive refinement during transient training. The steady solution is then independently assessed

against a finite-difference thermal benchmark before the transient baseline and parameter sweep are considered. This validation-before-sweep procedure provides a numerical check on the underlying thermo-fluid solution before the derived heat-transfer and entropy-generation trends are analyzed. The physical and computational parameters used in the present study are summarized in Table 1.

Table 1. Physical and computational parameters used in the present study.

Parameter	Symbol	Value
Channel length	L	2.0×10^{-3} m
Channel height	H	2.0×10^{-4} m
Channel aspect ratio	H/L	0.10
Reference inlet velocity	U_0	0.05 m/s
Applied wall heat flux	q''	2.0×10^4 W/m^2
Reference temperature	T_{ref}	300 K
Base fluid	—	Water
Base-fluid density	ρ_f	997.1 kg/m^3
Base-fluid specific heat	$c_{p,f}$	4179 J/(kg K)
Base-fluid thermal conductivity	k_f	0.613 W/(m K)
Base-fluid dynamic viscosity	μ_f	8.9×10^{-4} Pa·s
Al_2O_3 density	$\rho_{Al_2O_3}$	3970 kg/m^3
Al_2O_3 specific heat	c_{p,Al_2O_3}	765 J/(kg K)
Al_2O_3 thermal conductivity	$k_{Al_2O_3}$	40 W/(m K)
Cu density	ρ_{Cu}	8933 kg/m^3
Cu specific heat	$c_{p,Cu}$	385 J/(kg K)
Cu thermal conductivity	k_{Cu}	400 W/(m K)
Al_2O_3 volume fraction	ϕ_1	0.005, 0.010, 0.015
Cu volume fraction	ϕ_2	0.005, 0.010, 0.015
Pulsation amplitude	A	0, 0.2, 0.4
Pulsation frequency	f	10, 20, 40 Hz

Note: ϕ_1 denotes the Al_2O_3 nanoparticle volume fraction and ϕ_2 denotes the Cu nanoparticle volume fraction. In the completed parameter sweep, these fractions were varied as paired levels, i.e., $(\phi_1, \phi_2) = (0.005, 0.005)$, $(0.010, 0.010)$, and $(0.015, 0.015)$, rather than as independent phase parameters. The pulsation amplitude and frequency were varied over $A = 0$–0.4 and $f = 10$–40 Hz, respectively. The case $A = 0$ represents the non-pulsating reference condition; therefore, frequency does not have a physical effect on the inlet condition when $A = 0$.

The upper portion, as illustrated in Figure 1, shows the two-dimensional channel, pulsating inlet, heated lower wall, adiabatic upper wall, and downstream outlet conditions. The lower portion summarizes the computational sequence from physical formulation and nondimensional scaling through PINN construction, residual-based adaptive refinement, independent steady-state validation, transient pulsation analysis, parameter screening, and Pareto-based assessment.

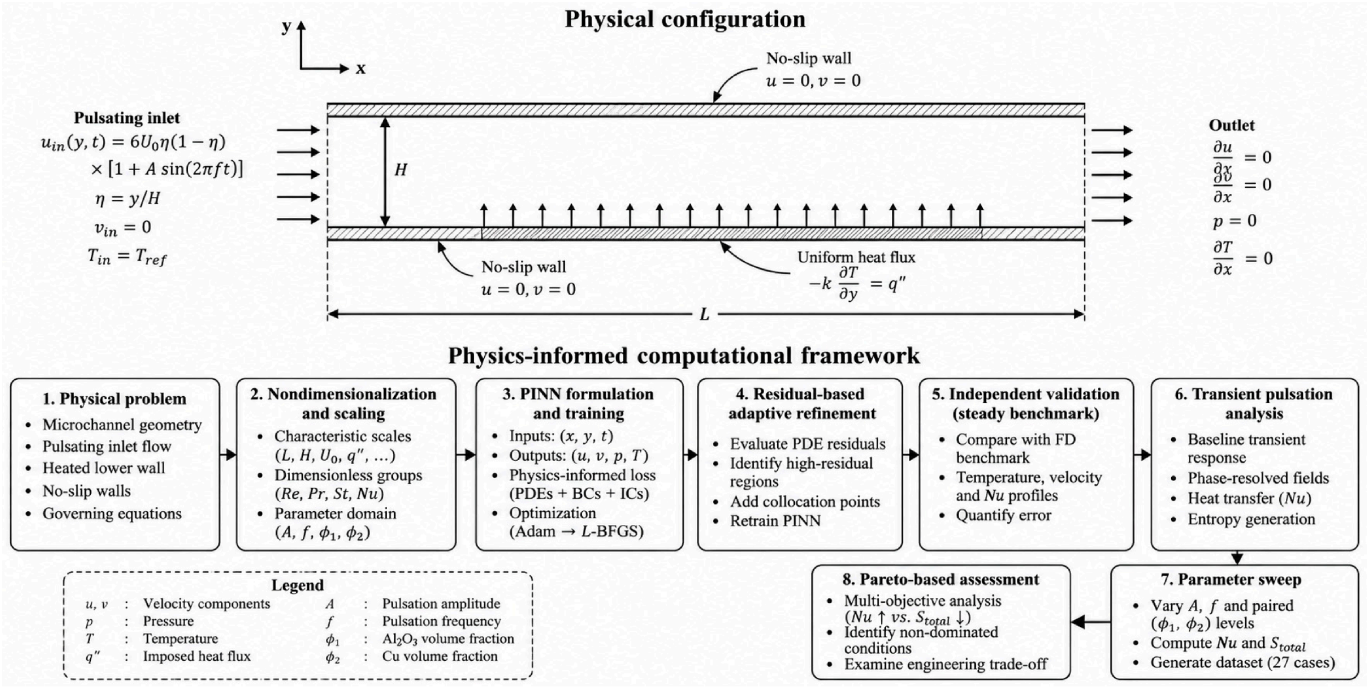


Figure 1. Schematic of the physical microchannel and the physics-informed computational workflow.

Governing equations

The transient thermo-fluid behavior in the microchannel is governed by the two-dimensional, incompressible continuity, momentum, and energy equations. The velocity field is represented by the streamwise and transverse components, $u(x,y,t)$ and $v(x,y,t)$, respectively. The physical pressure and temperature fields are denoted by $p(x,y,t)$ and $T(x,y,t)$.

For an incompressible fluid, conservation of mass is expressed as

$$\frac{\partial u}{\partial x} + \frac{\partial v}{\partial y} = 0. \tag{1}$$

The momentum equations are

$$\frac{\partial u}{\partial t} + u\frac{\partial u}{\partial x} + v\frac{\partial u}{\partial y} = -\frac{1}{\rho}\frac{\partial p}{\partial x} + \nu\left(\frac{\partial^2 u}{\partial x^2} + \frac{\partial^2 u}{\partial y^2}\right), \tag{2}$$

and

$$\frac{\partial v}{\partial t} + u\frac{\partial v}{\partial x} + v\frac{\partial v}{\partial y} = -\frac{1}{\rho}\frac{\partial p}{\partial y} + \nu\left(\frac{\partial^2 v}{\partial x^2} + \frac{\partial^2 v}{\partial y^2}\right), \tag{3}$$

where ρ is the fluid density and $\nu = \mu/\rho$ is the kinematic viscosity.

The temperature field is governed by the transient convection–diffusion equation,

$$\frac{\partial T}{\partial t} + u\frac{\partial T}{\partial x} + v\frac{\partial T}{\partial y} = \alpha\left(\frac{\partial^2 T}{\partial x^2} + \frac{\partial^2 T}{\partial y^2}\right), \tag{4}$$

where $\alpha = k/\left(\rho c_p\right)$ is the thermal diffusivity.

For consistency with the implemented PINN, the governing equations are nondimensionalized using

$$X = \frac{x}{L}, Y = \frac{y}{L}, \tau = \frac{tU_0}{L},$$

with U_0 as the reference velocity. The corresponding dimensionless velocity, pressure, and temperature variables are denoted by U, V, P, and Θ, respectively. The principal dimensionless groups are

$$Re = \frac{U_0 L}{\nu}, Pr = \frac{\nu}{\alpha}, St = \frac{fL}{U_0}.$$

Using these definitions, the residuals evaluated by the PINN are

$$R_c = \frac{\partial U}{\partial X} + \frac{\partial V}{\partial Y}, \tag{5}$$

$$R_u = St\frac{\partial U}{\partial \tau} + U\frac{\partial U}{\partial X} + V\frac{\partial U}{\partial Y} + \frac{\partial P}{\partial X} - \frac{1}{Re}\left(\frac{\partial^2 U}{\partial X^2} + \frac{\partial^2 U}{\partial Y^2}\right), \tag{6}$$

$$R_v = St\frac{\partial V}{\partial \tau} + U\frac{\partial V}{\partial X} + V\frac{\partial V}{\partial Y} + \frac{\partial P}{\partial Y} - \frac{1}{Re}\left(\frac{\partial^2 V}{\partial X^2} + \frac{\partial^2 V}{\partial Y^2}\right), \tag{7}$$

and

$$R_T = St\frac{\partial \Theta}{\partial \tau} + U\frac{\partial \Theta}{\partial X} + V\frac{\partial \Theta}{\partial Y} - \frac{1}{Re\,Pr}\left(\frac{\partial^2 \Theta}{\partial X^2} + \frac{\partial^2 \Theta}{\partial Y^2}\right). \tag{8}$$

For the steady benchmark, the temporal derivatives are suppressed by setting $St = 0$, consistent with the implementation. The four residuals in Equations (5)–(8) are evaluated through automatic differentiation of the neural-network outputs with respect to X, Y, and τ. The physics loss is constructed from the mean-square values of these residuals and is combined with the boundary and initial-condition losses. The implemented loss therefore constrains the predicted solution simultaneously through mass conservation, momentum conservation, energy transport, and the prescribed physical conditions rather than relying on labeled field data alone. This formulation follows the general physics-informed framework for differential-equation problems [27] and subsequent developments in physics-informed fluid mechanics [28–32]. Residual-based adaptive refinement is additionally used to introduce collocation points in regions where the governing-equation residuals remain relatively high [30]. The Maxwell-type thermal-conductivity relation and Brinkman viscosity model are adopted to represent the effective thermo-physical properties of the hybrid nanofluid under the conditions considered in this study. The calculations assume a homogeneous, single-phase suspension with relatively low total nanoparticle loading, with $\phi_1 + \phi_2 = 0.01$–0.03. Under these conditions, these classical effective-property relations provide a consistent first-order representation of the mixture thermal conductivity and dynamic viscosity while keeping the constitutive description compatible with the present continuum formulation. They are therefore used as constitutive approximations for the investigated concentration range rather than as universal models for all hybrid-nanofluid concentrations, particle interactions, or flow regimes.

2.2. Pulsating Inlet Condition

The transient behavior is introduced through a time-dependent inlet velocity. Importantly, the implemented model does **not** include an independent inlet phase parameter. The streamwise inlet velocity is prescribed as a parabolic profile whose magnitude is modulated periodically:

$$u_{\text{in}}(y,t) = 6\eta(1-\eta)[1 + A\sin(2\pi St\ \tau)], \tag{9}$$

where A is the dimensionless pulsation amplitude, f is the dimensional pulsation frequency, and

$$St = \frac{fH}{U_{\text{ref}}}$$

is the corresponding Strouhal number. Here, η represents the normalized transverse coordinate, and the factor $6\eta(1-\eta)$ defines the fully developed parabolic inlet profile used in the numerical implementation.

The transverse inlet velocity and dimensionless inlet temperature are prescribed as

$$v_{\text{in}} = 0$$

and

$$\theta_{\text{in}} = 0,$$

corresponding to zero transverse velocity and the reference inlet temperature, respectively. These conditions are imposed directly through the PINN boundary loss.

The investigated pulsation amplitudes are

$$A = 0.0,\ 0.2,\ 0.4,$$

while the forcing frequencies are

$$f = 10,\ 20,\ 40\ \text{Hz}.$$

The selected amplitude range of $0.0 - 0.4$ spans the non-pulsating reference condition and moderate inlet-velocity modulation. At the upper amplitude, $A = 0.4$, the prescribed modulation factor varies between 0.6 and 1.4, providing a bounded range of pulsation strengths for the present numerical investigation. The frequency range of 10–40 Hz was selected to provide low-, intermediate-, and higher-frequency forcing within the transient regime considered. These ranges are intended for systematic numerical screening of amplitude–frequency effects rather than to represent the complete operating envelope of pulsating microchannels.

When $A = 0$, Equation (9) reduces to the non-pulsating parabolic inlet profile,

$$u_{\text{in}}(y,t) = 6\eta(1-\eta),$$

and the physical inlet condition is therefore independent of the specified frequency. Accordingly, the $A = 0$ cases are treated as non-pulsating reference conditions rather than as physically frequency-dependent inlet states. This distinction is important when interpreting the subsequent parameter sweep.

The nanoparticle volume fractions are defined separately from the pulsation parameters. Specifically, ϕ_1 denotes the Al_2O_3 volume fraction and ϕ_2 denotes the Cu volume fraction. In the completed parameter sweep, these concentrations are varied as paired levels,

$$(\phi_1, \phi_2) = (0.005, 0.005),\ (0.010, 0.010),\ (0.015, 0.015),$$

rather than as independent variables. These quantities enter the effective thermophysical-property model and are not phase offsets in the pulsating inlet condition.

The time-dependent inlet condition produces an evolving velocity field and associated temperature field. The transient response is resolved directly through the temporal coordinate of the PINN rather than by solving a separate steady problem at each phase. The baseline transient case uses

$$A = 0.30, f = 20\ \text{Hz},$$

and is evaluated at representative phases of the final trained pulsation cycle. The corresponding Nusselt numbers are 5.0435, 4.8684, 4.6994, and 4.5413 at phases $\tau = 0.00,\ 0.25,\ 0.50$, and 0.75, respectively. Thus, over the evaluated phase interval, the Nusselt number decreases by 9.96%. The corresponding total entropy-generation rates are

$$3.8629 \times 10^{-4},\ 3.9992 \times 10^{-4},\ 4.1448 \times 10^{-4},\ 4.2938 \times 10^{-4}\ \text{W/K},$$

respectively, representing an 11.16% increase from $\tau = 0.00$ to $\tau = 0.75$.

These results demonstrate that both heat-transfer performance and entropy generation vary over the pulsation cycle. Consequently, assessment based solely on a single instantaneous heat-transfer value may not fully represent the associated thermodynamic response. The transient formulation therefore provides the basis for evaluating the coupled

variation of Nu and total entropy generation before examining the broader amplitude–frequency–composition parameter space. The subsequent parameter sweep and Pareto analysis are consequently formulated as a discrete screening of the tested operating conditions, rather than as a continuous optimization over an unrestricted parameter space.

2.3. Boundary and Initial Conditions

The boundary conditions are imposed together with the governing-equation residuals so that the PINN satisfies the physical constraints of the microchannel during training. At the inlet, the streamwise velocity is prescribed using the pulsating parabolic profile given in Equation (9), while the transverse velocity is set to zero. The dimensionless inlet temperature is fixed at the reference temperature. No-slip conditions are imposed at both channel walls. The lower wall is subjected to a uniform heat flux, while the upper wall is maintained as adiabatic. Because the spatial coordinates are nondimensionalized using the channel length, the corresponding wall-normal temperature-gradient conditions are imposed in their dimensionless form. At the outlet, the pressure is fixed at the reference value, together with zero streamwise gradients for the velocity and temperature fields. For the transient simulations, the initial state is taken as the unmodulated inlet condition with zero transverse velocity and the reference temperature. This provides a consistent starting state before the imposed pulsation develops. Importantly, the initial condition is not assigned a separate forcing phase; the subsequent temporal evolution is determined directly by the time coordinate of the transient PINN. The implementation therefore applies the prescribed inlet profile when constructing the initial-condition loss. All boundary and initial conditions are incorporated into the composite PINN loss, with the inlet, outlet, wall, and initial-condition contributions evaluated separately. This separation is important because a low total loss alone does not guarantee that every individual physical constraint has been adequately satisfied.

2.4. Dimensionless Formulation and Characteristic Parameters

The computational domain is nondimensionalized using the channel length and reference velocity. The spatial and temporal coordinates are defined as

$$X = \frac{x}{L}, Y = \frac{y}{L}, \tau = \frac{tU_0}{L},$$

where L is the channel length and U_0 is the reference inlet velocity. The dimensionless channel height is therefore

$$H^* = \frac{H}{L}.$$

The velocity components are scaled with U_0, while the temperature is nondimensionalized using the imposed wall heat flux and the thermal conductivity of the effective fluid,

$$\Theta = \frac{T - T_{\text{ref}}}{q'' L/k}.$$

The principal dimensionless flow and thermal parameters are the Reynolds and Prandtl numbers,

$$Re = \frac{U_0 L}{\nu}, Pr = \frac{\nu}{\alpha},$$

where ν is the effective kinematic viscosity and α is the effective thermal diffusivity. The pulsation frequency is represented through the Strouhal number,

$$St = \frac{fL}{U_0}.$$

The Strouhal number provides the connection between the dimensional forcing frequency used in the parameter study and the temporal coordinate of the transient formulation.

Heat-transfer performance is quantified using the Nusselt number,

$$Nu = \frac{q'' H}{k(T_w - T_b)},$$

where T_w is the heated-wall temperature and T_b is the velocity-weighted bulk temperature. The bulk temperature is evaluated from the cross-sectional velocity and temperature fields. Only spatial locations satisfying the required positive wall-to-bulk temperature difference and finite velocity-weighted denominator are retained in the Nusselt number calculation. For transient analysis, phase is used only as a convenient identifier for a point within the pulsation cycle and is not introduced as an additional model parameter. The baseline case is evaluated at four representative phases of the final trained cycle, whereas the parameter sweep is evaluated at the midpoint of the final cycle, corresponding to phase 0.50.

2.5. Physics-Informed Neural-Network Architecture and Training

The coupled velocity, pressure, and temperature fields are represented by a fully connected physics-informed neural network. The network receives the dimensionless coordinates

$$(X, Y, \tau)$$

as inputs and predicts the four dimensionless field variables

$$(U, V, P, \Theta).$$

The implemented network contains five hidden layers with 128 neurons per layer, using the hyperbolic-tangent activation function. Xavier initialization is used for the trainable network weights. Spatial and temporal derivatives required by the governing equations are obtained through automatic differentiation and are substituted into the continuity, momentum, and energy equations to construct the corresponding physics residuals.

A fixed random seed of 42 is used throughout the calculations to improve reproducibility. The executable implementation sets the Python 3.13.15, NumPy2.1.3, and PyTorch 2.11.0+cu130 random seeds to 42 and also initializes the CUDA 13.0 random state when a GPU is available. No independent repeated-training ensemble was performed; the reported results correspond to the fixed-seed training realization used in the executable implementation. This should therefore be interpreted as a controlled reproducibility measure rather than as an assessment of variability across independent training runs. Training is performed in two stages. Adam is first used to establish the solution, followed by L-BFGS refinement. The training settings differ between the independent steady validation, transient baseline, and parameter-sweep calculations and are reported according to the executable implementation. For the steady benchmark, the network uses 10,000 Adam iterations and 800 L-BFGS iterations with 6000 initial collocation points. For the transient baseline, 12,000 Adam iterations and 900 L-BFGS iterations with 7000 initial collocation points are used. The transient training window covers four pulsation periods. For each of the 27 parameter-sweep configurations, the network uses 6000 Adam iterations and 600 L-BFGS iterations, starting from 5000 initial collocation points. The network is initially trained in single precision, after which the model is converted to double precision for the L-BFGS refinement. This two-stage procedure is retained for both steady and transient calculations. The reported initialization procedure, random-seed setting, iteration counts, and collocation-point numbers correspond to the executable implementation used to generate the results, thereby maintaining consistency between the computational procedure and the reported results.

2.6. Physics-Informed Loss Formulation

The network is trained by minimizing a composite loss that combines the governing-equation residuals with the boundary and initial-condition constraints. The total loss is written as

$$\mathcal{L} = \lambda_{\text{phys}}\mathcal{L}_{\text{phys}} + \lambda_{\text{in}}\mathcal{L}_{\text{in}} + \lambda_{\text{out}}\mathcal{L}_{\text{out}} + \lambda_{\text{bw}}\mathcal{L}_{\text{bw}} + \lambda_{\text{tw}}\mathcal{L}_{\text{tw}} + \lambda_{\text{IC}}\mathcal{L}_{\text{IC}},$$

where the individual terms represent the physics, inlet, outlet, lower-wall, upper-wall, and initial-condition losses, respectively.

The physics loss is constructed from the mean-square residuals of continuity, streamwise momentum, transverse momentum, and energy,

$$\mathcal{L}_{\text{phys}} = \text{MSE}(R_c) + \text{MSE}(R_u) + \text{MSE}(R_v) + \text{MSE}(R_T).$$

The boundary terms measure the mismatch between the predicted fields and the prescribed boundary values or derivatives. The inlet contribution includes the prescribed streamwise and transverse velocities and inlet temperature, while the outlet contribution includes the pressure and zero-gradient conditions. The lower- and upper-wall terms include the corresponding no-slip and thermal conditions. The initial-condition term measures the mismatch between the predicted transient field and the prescribed initial state.

The implemented relative weights are

$$\boxed{\lambda_{\text{phys}} = 1, \lambda_{\text{in}} = 10, \lambda_{\text{out}} = 5, \lambda_{\text{bw}} = 15, \lambda_{\text{tw}} = 15, \lambda_{\text{IC}} = 10}$$

and therefore

$$\boxed{\mathcal{L} = \mathcal{L}_{\text{phys}} + 10\mathcal{L}_{\text{in}} + 5\mathcal{L}_{\text{out}} + 15\mathcal{L}_{\text{bw}} + 15\mathcal{L}_{\text{tw}} + 10\mathcal{L}_{\text{IC}}.}$$

The governing-equation residuals are assigned unit weight, while larger weights are applied to the boundary and initial conditions so that the prescribed physical constraints remain sufficiently enforced during optimization. The weighting was selected as a practical fixed-loss-balancing strategy for the present coupled thermo-fluid problem rather than as a separately optimized hyperparameter set. The same formulation allows the individual residual contributions to be monitored rather than relying solely on the magnitude of the total loss.

This distinction is important because a low composite loss does not, by itself, establish the accuracy of the resulting thermo-fluid fields. Accordingly, the steady solution is subsequently assessed against an independent numerical benchmark.

2.7. Residual-Based Adaptive Refinement

Because the governing-equation residual is not necessarily distributed uniformly throughout the computational domain, the transient calculations employ residual-based adaptive refinement (RAR). The purpose of RAR is to add collocation points in regions where the current PINN solution exhibits comparatively large, combined residuals. The procedure begins with an initial collocation set. During Adam training, candidate points are sampled within the computational domain and evaluated using the four governing-equation residuals. A combined residual score is then calculated, and the candidate points with the largest scores are retained as additional collocation points. The network subsequently continues training using the augmented collocation set. For the transient baseline, refinement is performed every 4000 Adam iterations. At each refinement stage, 4000 candidate points are evaluated and the 1000 highest-residual points are added to the retained training set. For the parameter sweep, refinement is performed every 3000 Adam iterations, with 3000 candidate points evaluated and the 750 highest-residual points added at each

refinement stage. This adaptive procedure allows the collocation distribution to respond to the evolving transient solution rather than remaining completely fixed throughout training. It is particularly useful for the present pulsating-flow problem because the velocity and temperature fields vary with the imposed oscillation. RAR is used strictly as a numerical refinement procedure and is not treated as a substitute for independent validation.

2.8. Heat-Transfer and Thermodynamic Metrics

The thermal performance of the microchannel is evaluated primarily using the Nusselt number. The local value is calculated from the imposed wall heat flux, channel height, thermal conductivity, wall temperature, and velocity-weighted bulk temperature:

$$Nu_x = \frac{q'' H}{k[T_w(x) - T_b(x)]}. \tag{10}$$

The bulk temperature is obtained from the predicted velocity and temperature fields using

$$T_b(x) = \frac{\int_0^H uT\, dy}{\int_0^H u\, dy}. \tag{11}$$

This velocity-weighted definition is appropriate for the internal forced-convection configuration considered here. The code evaluates the local Nusselt number along the heated wall and calculates the mean value from the valid locations. Heat transfer is complemented by an entropy-generation analysis to account for the thermodynamic cost associated with the transport process. The local entropy-generation rate is separated into thermal and viscous contributions:

$$s_{\text{gen}} = s_{\text{th}} + s_{\text{vis}}, \tag{12}$$

where

$$s_{\text{th}} = \frac{k}{T^2}\left[\left(\frac{\partial T}{\partial x}\right)^2 + \left(\frac{\partial T}{\partial y}\right)^2\right], \tag{13}$$

and

$$s_{\text{vis}} = \frac{\mu}{T}\left[2\left(\frac{\partial u}{\partial x}\right)^2 + 2\left(\frac{\partial v}{\partial y}\right)^2 + \left(\frac{\partial u}{\partial y} + \frac{\partial v}{\partial x}\right)^2\right]. \tag{14}$$

The resulting local quantity has units of W m^{-3} K^{-1}. The total entropy-generation rate is obtained by integrating the local generation rate over the complete channel volume,

$$S_{\text{total}} = \int_0^L \int_0^H s_{\text{gen}}\, dy\, dx, \tag{15}$$

and is therefore reported in W K^{-1}. The thermal and viscous contributions are integrated separately in the same manner. This distinction between the local entropy-generation density and the integrated total entropy-generation rate is maintained throughout the analysis. The simultaneous consideration of Nu and S_{total} provides a more complete description of the transient response than heat transfer alone. For the baseline transient case ($A, = 0.30 f = 20$ Hz), the solution was evaluated at phases 0.00, 0.25, 0.50, and 0.75 of the final trained cycle. The corresponding Nusselt numbers were 5.0435, 4.8684, 4.6994, and 4.5413, respectively. Thus, Nu decreased by approximately 9.96% from phase 0.00 to phase 0.75. Over the same interval, the total entropy-generation rate increased from

$$3.86292 \times 10^{-4}$$

to

$$4.29383 \times 10^{-4}\ \text{W K}^{-1},$$

corresponding to an increase of approximately 11.16%.

These phase-resolved results illustrate that heat-transfer performance and entropy generation do not necessarily vary in the same direction during a pulsation cycle. The subsequent parameter study therefore considers both quantities when comparing the tested operating conditions. For the systematic parameter study, the pulsation amplitude was varied over $A = 0$, 0.2, and 0.4, while the frequency was varied over 10, 20, and 40 Hz. The selected amplitude range $A = 0$–0.4 spans the non-pulsating reference condition and moderate inlet-velocity modulation. At the upper amplitude $A = 0.4$, the prescribed modulation factor $1 + A\sin(2\pi St\tau)$ varies between 0.6 and 1.4, providing a bounded range of pulsation strengths for the present numerical investigation. The frequency range of 10–40 Hz was selected to provide low-, intermediate-, and higher-frequency forcing within the transient regime considered in this study. These ranges are intended for systematic numerical screening of amplitude–frequency effects rather than to represent the complete operating envelope of pulsating microchannels. The $A = 0$ cases require a specific interpretation. When $A = 0$, the inlet condition reduces to the non-pulsating velocity profile and is independent of frequency. Consequently, the nominal 10, 20, and 40 Hz cases at $A = 0$ do not represent physically different forcing frequencies; they serve as separate numerical realizations of the same non-pulsating reference condition. For the sweep, each trained transient model is evaluated at the midpoint of its final pulsation cycle (phase 0.50). A case is considered numerically reliable when at least 90% of the evaluated wall locations provide valid Nusselt values and both Nu and S_{total} are finite. The resulting dataset is then used for the Pareto-based assessment. Because the present study evaluates a finite set of 27 completed configurations, the resulting non-dominated conditions are interpreted within the tested amplitude, frequency, and paired-composition ranges, rather than as a universal or continuous optimum. A finer parameter sweep could identify additional non-dominated conditions between the discrete cases considered here.

3. PINN Training and Independent Validation

A physics-informed model is useful for subsequent parameter studies only when its solution has first been checked against an independent numerical reference. Accordingly, the present study separates the steady-model validation stage from the subsequent transient and parametric calculations. The steady thermo-fluid problem was solved first using the PINN, and the resulting fields were compared with an independently implemented finite-difference (FD) benchmark. The comparison was made for the temperature and velocity fields, as well as for the derived Nusselt number. This approach provides a more meaningful assessment than relying on the training loss alone. A low optimization loss indicates that the selected residuals have been reduced during training, but it does not by itself demonstrate that the predicted fields or derived engineering quantities are accurate. The independent comparison therefore serves as the main validation step before the trained framework is extended to the transient pulsating cases.

3.1. Steady-State PINN Training and Convergence

The steady reference solution was obtained using the same PINN architecture and governing equations described in Section 2. The model was trained in two stages. Adam was first used to obtain a stable solution, after which the network was converted to double precision and refined using L-BFGS. For the steady validation case, the executable implementation used 10,000 Adam iterations, 800 L-BFGS iterations, and 6000 initial collocation points. No residual-based adaptive refinement was applied during this steady validation stage. The convergence history is shown in Figure 2. Rather than using the final value of the total loss as the sole convergence indicator, the evolution of the total,

physics, and boundary-condition losses was monitored throughout training. The Adam stage establishes the initial solution and progressively reduces the governing-equation and constraint residuals. The subsequent L-BFGS stage provides further refinement of the already trained solution. Small fluctuations in individual residual components can occur during optimization because the physics, boundary, and initial-condition terms are minimized simultaneously. The convergence history is therefore interpreted together with the independent validation results rather than in isolation. In particular, the purpose of the training stage is to obtain a numerically stable field representation that satisfies the governing equations and imposed constraints sufficiently well for independent comparison. To provide an explicit numerical screening criterion, the implementation applies a validation gate before the transient calculations are allowed to proceed. A steady solution is accepted when the valid Nusselt number fraction is at least 90%, while the relative errors in the temperature profile, velocity profile, and downstream Nusselt number are each below 10%. These limits are used as computational acceptance criteria rather than as claims of experimental accuracy. The independent FD comparison subsequently provides the more direct test of predictive accuracy. The validated steady PINN reproduced the temperature profile with a relative error of 0.08% and the velocity profile with a relative error of 0.04%. The downstream Nusselt number predicted by the PINN was 2.9969, compared with 2.8953 from the independent FD calculation, giving a relative difference of 3.51%. These results indicate close agreement for the primary thermo-fluid fields and a small discrepancy in the derived heat-transfer quantity. The somewhat larger error in Nu is expected to be more sensitive to the reconstructed temperature field and its wall-level gradient than the direct profile comparisons. Importantly, the FD solution was not used as training data; it was generated independently and was used only for validation. Thus, the training-loss history is treated as evidence of numerical convergence, while the independent FD comparison provides the principal evidence supporting the use of the steady PINN as the starting point for the subsequent transient analysis.

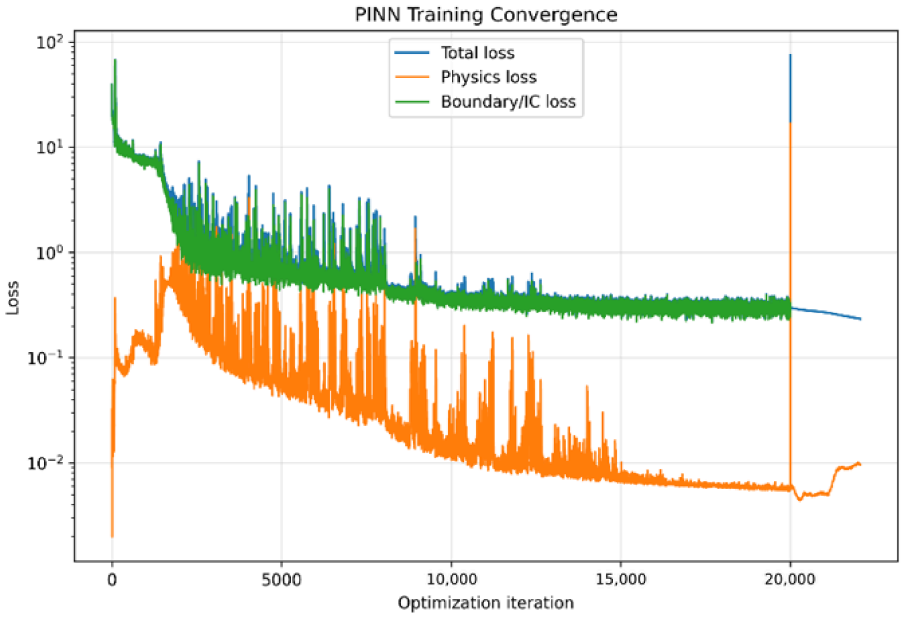


Figure 2. PINN training convergence for the steady thermo-fluid problem. The total loss, physics loss, and combined boundary-condition loss are shown on a logarithmic scale. The initial Adam stage establishes the solution, followed by L-BFGS refinement. Despite local residual fluctuations during optimization, the overall loss envelope decreases substantially and reaches a comparatively stable regime before independent validation.

3.2. Independent Validation of Temperature and Velocity Fields

After training, the steady PINN solution was assessed against two independent reference solutions. The temperature field was compared with an independently calculated finite-difference (FD) solution that was not used during network training, thereby providing an independent numerical benchmark. The axial velocity field was evaluated against the analytical fully developed parabolic velocity profile expected for the present channel-flow configuration. In both cases, the comparison was performed over the complete profiles rather than at a single representative location. Figure 3a shows the temperature profiles predicted by the PINN and obtained from the independent FD calculation. The two profiles exhibit close agreement across the channel height, with a profile-level relative error of only 0.08%. The representative values reported in Table 2 are 302.70 K for the PINN and 302.46 K for the FD solution. These values are included to indicate the magnitude of the temperature field; the reported 0.08% error is calculated from the complete temperature profiles rather than from the individual tabulated values.

Table 2. Steady-state validation of the PINN solution.

Quantity	PINN Result	Independent Reference	Relative Error/Difference
Temperature profile	302.70 K	302.46 K (FD)	**0.08%**
Velocity profile	0.05000 m/s	0.04998 m/s (analytical parabolic)	**0.04%**
Downstream Nusselt number	2.9969	2.8953 (FD)	**3.51%**

Note: The temperature profile and downstream Nusselt number are compared with the independent finite-difference (FD) benchmark, whereas the velocity profile is compared with the analytical fully developed parabolic velocity distribution. The relative errors are calculated with respect to the corresponding reference values.

The corresponding axial velocity profiles are presented in Figure 3b. The PINN accurately reproduces the characteristic fully developed channel-flow distribution, with the velocity decreasing toward the walls and reaching its maximum in the channel interior. Comparison with the analytical fully developed parabolic reference gives representative velocities of 0.05000 m/s for the PINN and 0.04998 m/s for the analytical solution, corresponding to a profile-level relative error of 0.04%. This close agreement confirms that the hydrodynamic field predicted by the PINN is consistent with the expected fully developed flow behavior. Agreement in both temperature and velocity is important because the subsequent heat-transfer analysis depends on their coupled behavior. Agreement on temperature alone would not establish that the underlying hydrodynamic solution has also been reproduced correctly, while agreement on velocity alone would not demonstrate that the corresponding thermal transport is accurately captured. The close agreement obtained for both fields therefore provides a consistent numerical verification of the steady thermo-fluid solution before applying the PINN framework to the transient pulsating-flow cases. The validation is intentionally reported at the profile level. The representative values listed in Table 2 should not be interpreted as independent pointwise validation metrics; rather, they provide reference values for the compared fields. The quoted relative errors are calculated from the corresponding complete profiles, providing a more representative measure of agreement and avoiding overinterpretation of individual tabulated values.

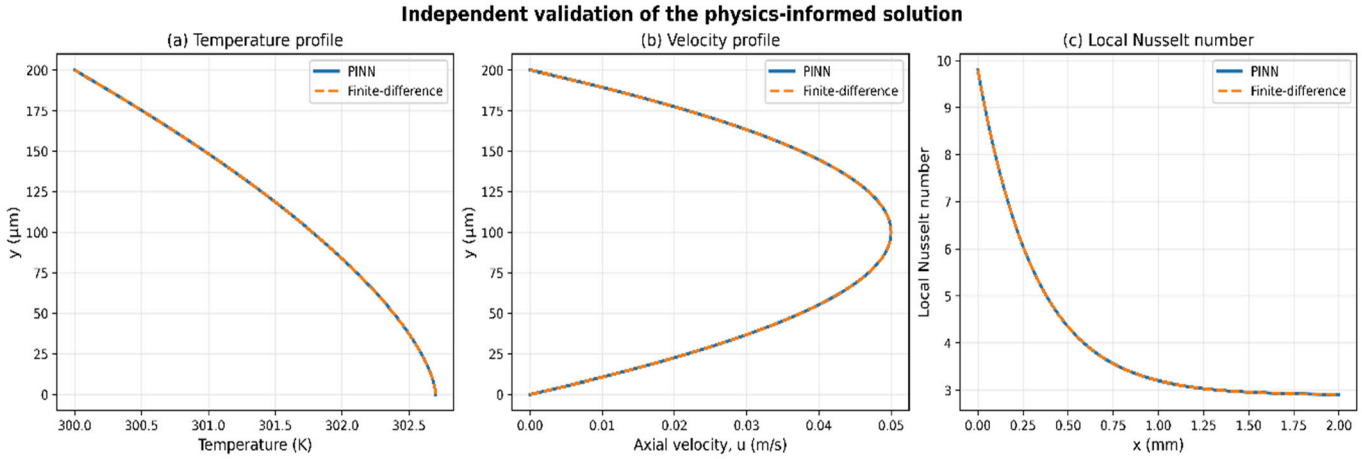


Figure 3. Independent validation of the steady PINN solution. (**a**) Temperature profile predicted by the PINN and compared with the independent finite-difference (FD) benchmark. (**b**) Axial velocity profile predicted by the PINN and compared with the analytical fully developed parabolic reference. (**c**) Local Nusselt number distribution along the channel from the PINN and independent FD calculation. The close agreement between the PINN predictions and their corresponding reference solutions demonstrates consistency in the primary thermo-fluid fields and the derived heat-transfer response.

3.3. Validation of the Derived Nusselt Number Response

In addition to the primary velocity and temperature fields, the PINN was assessed using the Nusselt number calculated from the predicted thermal field. This provides a useful additional check because Nu is a derived heat-transfer quantity and is more sensitive to differences in the thermal field and wall-temperature gradients than the direct field comparisons. As shown in Figure 3c, the PINN and FD calculations exhibit the same overall spatial variation in the local Nusselt number. The local heat-transfer coefficient is higher in the developing region and decreases along the channel toward the downstream region. The two predictions remain closely comparable over the evaluated streamwise range.

For the downstream region, the PINN gives

$$Nu_{\mathrm{PINN}} = 2.9969,$$

whereas the independent FD calculation gives

$$Nu_{\mathrm{FD}} = 2.8953.$$

The resulting relative difference is

$$\frac{|\,2.9969 - 2.8953\,|}{2.8953} \times 100 = 3.51\%.$$

The Nusselt number discrepancy is larger than the errors obtained for the direct temperature and velocity profiles. This is not unexpected because Nu is derived from the thermal field and therefore depends on quantities such as the wall temperature and temperature gradient. Small differences in the reconstructed thermal field can consequently become more apparent when a gradient-dependent heat-transfer quantity is calculated. Nevertheless, the 3.51% difference in the downstream Nusselt number, together with the 0.08% temperature-profile error and 0.04% velocity-profile error, provides an independent check of both the primary solution fields and a key engineering quantity used in the subsequent analysis. The comparison is therefore used to establish the numerical reliability of the steady PINN before proceeding to the transient pulsation calculations. It is important to distinguish this steady validation from the transient analysis that follows. The present study uses an

independent FD benchmark for the steady reference problem; an independent transient CFD/FD benchmark is not performed for every pulsating configuration. The transient results are therefore interpreted within the validated computational framework and are additionally screened using the residual and validity checks described in the methodology. This limitation is explicitly recognized rather than treating the steady benchmark as a direct validation of every transient case.

3.4. Validation Assessment and Transition to Transient Pulsation

The steady PINN solution was assessed against two independent numerical references, with the comparison performed separately for the primary flow and thermal quantities. The temperature profile agrees with the independent finite-difference (FD) benchmark with a relative error of 0.08%, while the downstream Nusselt number is 2.9969 for the PINN and 2.8953 for the FD solution, corresponding to a relative difference of 3.51%. The velocity profile, in contrast, was compared with the analytical fully developed parabolic reference and shows a relative error of 0.04%. Thus, the two primary field comparisons remain below 0.1%, while the derived heat-transfer quantity differs from the independent FD benchmark by only a few percent. Before proceeding to the transient calculations, the code applies an explicit numerical validation gate. The steady solution is accepted only when at least 90% of the evaluated Nusselt number points are valid and the relative errors in temperature, velocity, and downstream Nusselt number are each below 10%. These limits are used solely as computational acceptance criteria for the present study; they do not represent experimental uncertainty or a universal accuracy threshold. The obtained steady solution satisfies all three criteria and was therefore used as the starting point for the transient calculations. The steady benchmark is deliberately separated from the subsequent transient analysis. The FD calculation provides an independent reference for the steady temperature field and Nusselt number prediction, whereas the velocity field is assessed against the analytical fully developed parabolic solution. No independent FD or CFD benchmark was performed for every pulsation amplitude and frequency considered in the transient study. Accordingly, the steady comparison should not be interpreted as direct validation of every transient solution. Rather, it verifies that the governing equations, boundary conditions, field reconstruction, and heat-transfer post-processing reproduce established reference solutions before the framework is extended to the transient problem. This comparison also does not imply that the PINN is intrinsically more accurate than either reference. The FD solution and analytical velocity profile are used as independent reference solutions, and the purpose of the comparison is to quantify how closely the trained PINN reproduces them. The subsequent transient and parametric results are therefore interpreted as predictions obtained using a numerically verified computational framework rather than as results independently validated for every transient condition. Following the steady assessment, the model was extended to transient pulsating flow. The representative transient case uses $A = 0.30$ and $f = 20$ Hz, with the solution evaluated at four positions within the final trained pulsation cycle: $\tau = 0.00,\ 0.25,\ 0.50$, and 0.75. Here, τ denotes the normalized position within the pulsation cycle. These phase points are extracted directly from the final trained cycle rather than being introduced through an additional inlet-phase parameter. The phase-resolved calculation provides the first transient assessment of the framework by examining the evolution of the velocity and temperature fields together with the corresponding Nusselt number and total entropy generation. The subsequent parameter sweep then examines the effects of pulsation amplitude, frequency, and the prescribed paired nanoparticle-volume-fraction levels within the investigated parameter space. Importantly, these transient calculations are treated as an extension of the numerically verified steady

framework, rather than as independently benchmarked transient solutions. This distinction keeps the scope of the validation consistent with the calculations actually performed.

4. Transient Pulsating Baseline

4.1. Baseline Transient Solution

After establishing the steady solution and its agreement with the independent finite-difference benchmark, the PINN was extended to a representative transient pulsating condition. The purpose of this intermediate calculation was to examine whether the model produces a physically coherent phase-dependent response before the larger amplitude–frequency parameter sweep was performed.

The baseline case was defined using a pulsation amplitude of

$$A = 0.30$$

and a pulsation frequency of

$$f = 20 \text{ Hz}.$$

The nanoparticle volume fractions were fixed at the baseline values

$$\phi_1 = \phi_2 = 0.010$$

where ϕ_1 and ϕ_2 denote the Al_2O_3 and Cu volume fractions, respectively. The transient PINN was trained using 12,000 Adam iterations followed by 900 L-BFGS iterations, with 7000 initial collocation points and residual-based adaptive refinement during training.

The transient solution was evaluated at four positions within the final trained pulsation cycle,

$$\phi = 0, 0.25, 0.50, 0.75,$$

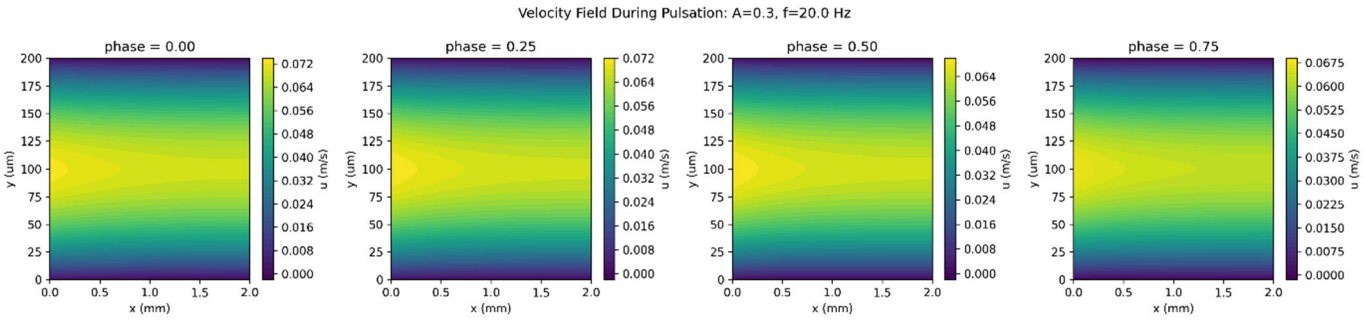
where ϕ denotes the normalized position within one pulsation period. These values are phase locations used for post-processing and are not additional inlet phase parameters. The inlet forcing itself is defined by the sinusoidal term in the governing boundary condition, while the phase values simply identify different points within the final computed cycle. This baseline calculation provides a transition between the steady validation and the broader parameter study. It allows the phase dependence of the predicted flow and thermal fields to be examined directly and provides a reference condition for interpreting the subsequent variations in pulsation amplitude and frequency. Because the independent FD comparison was performed only for the steady reference problem, the present transient calculation is treated as a phase-resolved numerical assessment of the trained PINN, rather than as an independently benchmarked transient solution.

4.2. Phase-Resolved Velocity and Temperature Fields

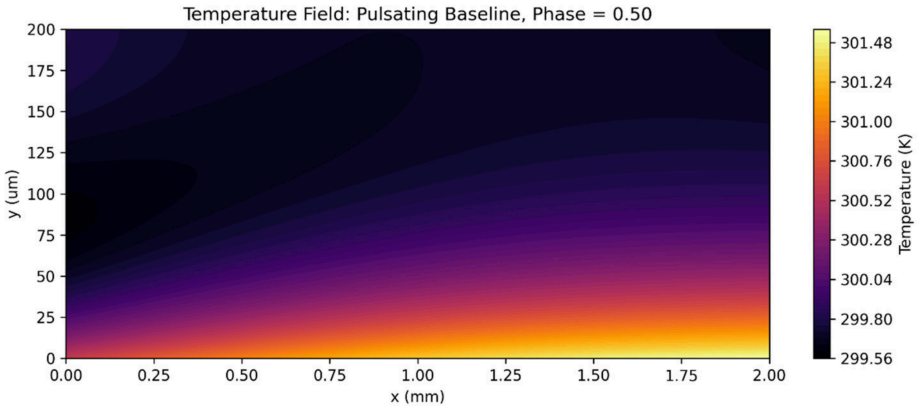
Figure 4 presents the phase-resolved thermo-fluid response of the baseline case (A= 0.30, f = 20 Hz). Figure 4a shows the axial velocity field at phases 0.00, 0.25, 0.50, and 0.75, while Figure 4b shows the temperature field at the representative phase 0.50.

The velocity fields retain the expected channel-flow structure throughout the pulsation cycle. The velocity remains close to zero at the no-slip walls and reaches its largest values within the channel interior. The primary phase-dependent change is therefore the magnitude of the velocity field rather than its overall spatial topology. For the imposed inlet profile, the maximum reference velocity at $A = 0$ is approximately 0.075 m/s, while the instantaneous velocity scale varies according to the prescribed sinusoidal inlet modulation. The four reported phases correspond to normalized positions within the final pulsation cycle rather than independent inlet phase parameters. For the baseline condition, the inlet modulation factor $1 + A\sin(2\pi St\tau)$ takes values of 1.00, 1.30, 1.00, and 0.70 at phases 0.00,

0.25, 0.50, and 0.75, respectively. Thus, the phase-resolved velocity fields represent the temporal response to the prescribed inlet modulation while retaining the same fundamental channel-flow structure. The differences between the fields should therefore be interpreted primarily as the changes in velocity magnitude associated with the pulsation cycle. The corresponding temperature distribution at phase 0.50 is shown in Figure 4b. The thermal field develops progressively along the heated channel, with higher temperatures occurring near the heated lower wall and toward the downstream region. The predicted distribution remains spatially smooth and follows the imposed lower-wall heat flux together with the convective transport generated by the evolving velocity field. The velocity and temperature fields do not respond identically to the imposed pulsation. The velocity responds directly to the time-dependent inlet forcing, whereas the temperature field reflects the combined effects of convection, thermal diffusion, and the applied wall heat flux. Consequently, the instantaneous thermal field does not simply mirror the instantaneous velocity magnitude; instead, the thermal response reflects the finite transport time associated with the evolving flow and temperature fields. The phase-resolved results therefore demonstrate that the transient PINN produces a coupled variation of the hydrodynamic and thermal fields over the pulsation cycle. This provides the basis for examining the corresponding phase dependence of the heat-transfer and entropy-generation metrics in the following section. The calculated Nusselt number decreases from 5.0435 at phase 0.00 to 4.5413 at phase 0.75, while all four evaluated phases satisfy a 100% valid Nusselt number fraction.



(**a**)



(**b**)

Figure 4. Phase-resolved thermo-fluid response of the PINN for the baseline condition ($A = 0.30$, $f = 20$ Hz). (**a**) Axial velocity fields at phases 0.00, 0.25, 0.50, and 0.75; (**b**) temperature field at phase 0.50.

4.3. Phase-Dependent Heat Transfer and Entropy Generation

The phase dependence of the transient response was quantified using the surface Nusselt number and the integrated total entropy-generation rate. The results obtained at four representative positions within the final pulsation cycle are summarized in Table 3.

Table 3. Phase-resolved baseline response for $A = 0.30$ and $f = 20$ Hz.

Phase, τ	Surface Nusselt Number, Nu	Total Entropy Generation, S_{gen} (W/K)	Valid Fraction
0.00	5.0435	3.8629×10^{-4}	100%
0.25	4.8684	3.9992×10^{-4}	100%
0.50	4.6994	4.1448×10^{-4}	100%
0.75	4.5413	4.2938×10^{-4}	100%

A clear phase dependence is observed in both quantities. The surface Nusselt number decreases from 5.0435 at $\tau = 0.00$ to 4.5413 at $\tau = 0.75$, corresponding to a 9.96% decrease. Over the same interval, the total entropy-generation rate increases from 3.8629×10^{-4} W/K to 4.2938×10^{-4} W/K, corresponding to an 11.16% increase. All four evaluated phases satisfy the numerical validity criterion, with a valid fraction of 100%. The intermediate phases follow the same progression: Nu decreases from 5.0435 to 4.8684, 4.6994, and 4.5413, while S_{gen} increases progressively over the same sequence. Thus, the two quantities exhibit opposite phase trends over the portion of the pulsation cycle examined. This difference is important because heat-transfer intensity and entropy generation describe different aspects of the instantaneous thermo-fluid state. The decrease in Nusselt number should not, however, be interpreted as being directly caused by the increase in entropy generation. Both quantities are evaluated from the evolving velocity and temperature fields and are influenced by the transient changes in convection, temperature gradients, and viscous dissipation. The baseline calculation therefore identifies an observed phase-dependent relationship between heat transfer and thermodynamic irreversibility, rather than establishing a direct causal relationship between the two.

The observed behavior is consistent with the broader understanding that pulsating flow can produce phase-dependent heat-transfer responses [15–19]. In the present framework, this response is evaluated together with the integrated entropy-generation rate, allowing the thermal performance and thermodynamic consequences of the transient flow to be examined within a common computational framework.

4.4. Physical Interpretation of the Baseline Response

The baseline calculation demonstrates that the transient response cannot be represented adequately by a single steady-state value. Across the four evaluated phases, the Nusselt number changes by approximately 10%, while the total entropy-generation rate changes by approximately 11%. These variations indicate that the instantaneous thermal performance and thermodynamic state evolve appreciably over the pulsation cycle. The phase dependence is particularly relevant when heat-transfer enhancement is considered together with irreversibility. A condition producing a larger instantaneous Nusselt number does not necessarily correspond to the same thermodynamic state as one producing a lower heat-transfer response. Entropy generation therefore provides complementary information that would be missed if the analysis were based on heat transfer alone. This treatment follows the broader entropy-generation approach used to assess heat-transfer performance together with thermodynamic irreversibility [20–26]. The baseline case consequently serves as the transition from phase-resolved transient analysis to the broader

parameter study. Rather than drawing conclusions from a single transient snapshot, the subsequent sweep examines different combinations of pulsation amplitude, frequency, and prescribed nanoparticle volume fractions. For the completed sweep, each configuration is evaluated at the midpoint of its final pulsation cycle, $\phi = 0.50$, and the resulting Nusselt number and entropy-generation rate are used for comparison and Pareto analysis. The resulting $Nu_s - S_{\text{total}}$ relationship provides the basis for identifying non-dominated conditions within the investigated parameter space, rather than defining a universal optimum. This distinction is important because the present sweep contains a finite set of 27 prescribed configurations, and the Pareto results are consequently limited to the range of amplitudes, frequencies, and nanoparticle concentrations examined in the study.

5. Parametric Effects of Pulsation

Following the baseline transient analysis, the influence of pulsation amplitude and frequency was examined over the completed parameter space. The purpose of this stage was not simply to determine whether stronger pulsation increases heat transfer but to examine how the combined forcing conditions alter the predicted heat-transfer response and the associated entropy generation. The pulsation amplitude is denoted by A, while the imposed frequency is represented by f. The completed sweep considered

$$A = 0,\ 0.2,\ 0.4$$

and

$$f = 10,\ 20,\ 40\ \text{Hz},$$

together with the three prescribed paired nanoparticle concentrations,

$$(\phi_1, \phi_2) = (0.005, 0.005),\ (0.010, 0.010),\ (0.015, 0.015).$$

This resulted in 27 completed configurations. For each configuration, the transient PINN was evaluated at the midpoint of the final trained pulsation cycle, corresponding to $\phi = 0.50$. The reported Nu_{mean} therefore represents the spatially averaged Nusselt response at this common phase location, rather than a full-cycle average. The same evaluation state was used to obtain the corresponding total entropy-generation rate. This procedure provides a consistent basis for comparing the different configurations without mixing the results obtained at different phases. A further point concerns the $A = 0$ cases. When $A = 0$, the inlet velocity is non-pulsating and is physically independent of the specified frequency. Thus, the $A = 0$ results are treated as non-pulsating reference calculations; differences between their numerical values at 10, 20, and 40 Hz should not be interpreted as a physical frequency effect on the inlet forcing. This distinction is important when interpreting the amplitude–frequency trends.

5.1. Effect of Pulsation Amplitude on Heat Transfer

Figure 5 illustrates the variation in the spatially averaged Nusselt number with pulsation amplitude at the three investigated frequencies using the intermediate nanoparticle concentration of $\phi_1 = \phi_2 = 0.010$. The results reveal a non-monotonic response that depends on the combination of amplitude and frequency, indicating that increasing pulsation strength does not necessarily improve heat transfer.

At 10 Hz, the non-pulsating reference ($A = 0$) gives a mean Nusselt number of 4.8387. Increasing the amplitude to $A = 0.2$ reduces this value to 3.9133, a decrease of approximately 19.1%. A further increase to $A = 0.4$, however, raises the Nusselt number to 5.3405, exceeding the reference value. The response at this frequency therefore decreases initially before increasing at the highest amplitude.

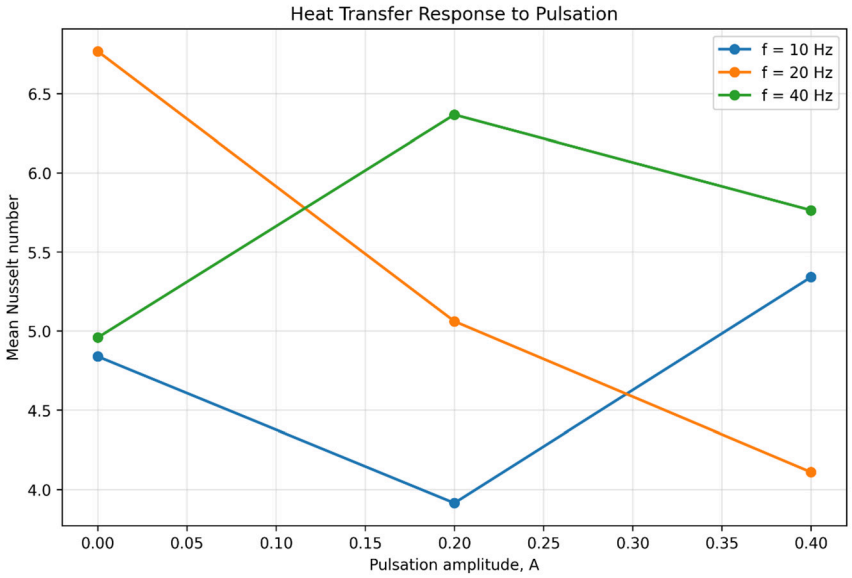


Figure 5. Effect of pulsation amplitude and frequency on mean heat transfer. Variation of Nu_{mean} with pulsation amplitude A for $f = 10$, 20, and 40 Hz. The distinctly different responses at the three frequencies demonstrate that heat-transfer performance depends on the coupled amplitude–frequency condition rather than on pulsation amplitude alone.

At 20 Hz, the mean Nusselt number decreases from 6.7670 at $A = 0$ to 5.0614 at $A = 0.2$ and 4.1088 at $A = 0.4$. These values represent reductions of approximately 25.2% and 39.3%, respectively, relative to the non-pulsating reference. Unlike the 10 Hz case, the predicted heat-transfer response decreases progressively with the increasing amplitude over the investigated range. A different trend is observed at 40 Hz. The reference Nusselt number of 4.9585 increases to 6.3668 at $A = 0.2$, corresponding to an enhancement of approximately 28.4%. Increasing the amplitude further to $A = 0.4$ reduces the Nusselt number to 5.7640, although it remains above the reference value. The highest heat-transfer response in this series therefore occurs at the intermediate amplitude rather than at the maximum amplitude considered. These differences suggest that the effectiveness of pulsation depends on the interaction between the imposed forcing and the characteristic transport timescales of the flow. Physically, the forcing frequency determines the time available for the hydrodynamic and thermal boundary layers to respond during each pulsation cycle. At lower frequencies, the velocity and temperature fields have more time to adjust to the imposed modulation. At higher frequencies, the forcing changes more rapidly relative to the characteristic momentum- and heat-transport timescales. The resulting interaction between pulsation, boundary-layer development, and thermal diffusion offers a qualitative explanation for the observed frequency-dependent and non-monotonic behavior [15–19]. However, because boundary-layer thicknesses and characteristic response times were not calculated independently, this interpretation is presented as a possible physical explanation rather than a directly verified mechanism.

Overall, the results demonstrate that pulsation amplitude and frequency must be considered together when assessing heat-transfer performance. An amplitude that improves heat transfer at one frequency may produce a less favorable response at another. The observed trends are therefore best interpreted as a parameter-dependent response within the investigated range, rather than as evidence of a universally beneficial pulsation amplitude. These findings also motivate the subsequent thermodynamic assessment. Although the Nusselt number describes the heat-transfer response, it does not independently quantify the associated thermodynamic irreversibility. The same operating conditions are therefore

examined in terms of total entropy generation in the following section, allowing heat-transfer performance and its thermodynamic cost to be evaluated together.

5.2. Effect of Pulsation Amplitude on Entropy Generation

The heat-transfer response alone does not fully describe the effect of pulsation, since changes in the flow field also modify the irreversible processes within the channel. The corresponding total entropy-generation rate, S_{total}, was therefore examined for the same parameter combinations used in Section 5.1. The total value is obtained from the thermal and viscous contributions,

$$S_{total} = S_{thermal} + S_{viscous},$$

where the two terms represent the irreversibility associated with temperature gradients and velocity gradients, respectively [20,23–26]. Figure 6 shows the variation of S_{total} with pulsation amplitude for $f = 10$, 20, and 40 Hz at $\phi_1 = \phi_2 = 0.010$. As with the heat-transfer results, the entropy-generation response is not monotonic and changes with the frequency. The values reported here correspond to the midpoint of the final trained pulsation cycle ($\phi = 0.50$), which was used consistently for all 27 parameter-sweep configurations. Thus, these values should be interpreted as phase-specific comparisons at a common cycle position rather than as cycle-averaged entropy-generation rates. At $f = 10$ Hz, S_{total} is approximately 4.78×10^{-4} W/K at $A = 0$, increases to approximately 5.78×10^{-4} W/K at $A = 0.2$, and then decreases to approximately 4.07×10^{-4} W/K at $A = 0.4$. The entropy-generation response therefore follows a non-monotonic pattern as the forcing amplitude is increased. At $f = 20$ Hz, the corresponding values are approximately 3.39×10^{-4}, 3.95×10^{-4}, and 5.33×10^{-4} W/K for $A = 0$, 0.2, and 0.4, respectively. In this case, entropy generation increases progressively with amplitude. A different behavior is observed at $f = 40$ Hz. The entropy-generation rate is approximately 4.08×10^{-4} W/K at $A = 0$, decreases to about 2.83×10^{-4} W/K at $A = 0.2$, and then increases slightly to approximately 3.17×10^{-4} W/K at $A = 0.4$. Thus, the intermediate amplitude produces the lowest entropy-generation value within this particular frequency series. These results show that entropy generation does not respond to pulsation amplitude in a universal manner. The direction and magnitude of the change depend on the forcing frequency, reflecting the combined effect of pulsation on the velocity and temperature gradients from which the thermal and viscous entropy-generation terms are calculated. The observed behavior is therefore consistent with the coupled nature of heat transfer and irreversible transport in pulsating flows [20,24–26]. The comparison with the Nusselt number results also illustrates why the two quantities should be considered together. For example, at $\phi_1 = \phi_2 = 0.010$, the $A = 0.2$, $f = 40$ Hz condition gives a relatively high Nu_{mean} of 6.3668 while also giving the lowest entropy-generation value among the three amplitudes examined at that frequency. This does not, by itself, establish a global optimum, since the complete sweep also varies nanoparticle concentration and contains other configurations. Indeed, the full 27-case dataset identifies $A = 0.2$, $f = 20$ Hz, $\phi_1 = \phi_2 = 0.015$ as the configuration having both the highest reported Nu_{mean} (7.1126) and the lowest reported S_{total} (2.7496×10^{-4} W/K) within the completed parameter space. The entropy-generation results therefore reinforce the main point of the parametric analysis: pulsation amplitude cannot be assessed independently of frequency or thermal performance. A change that improves heat transfer under one condition may have a different thermodynamic consequence under another. Accordingly, the subsequent analysis treats Nu_{mean} and S_{total} as simultaneous performance measures and uses the completed 27-case dataset to identify non-dominated conditions through a Pareto analysis.

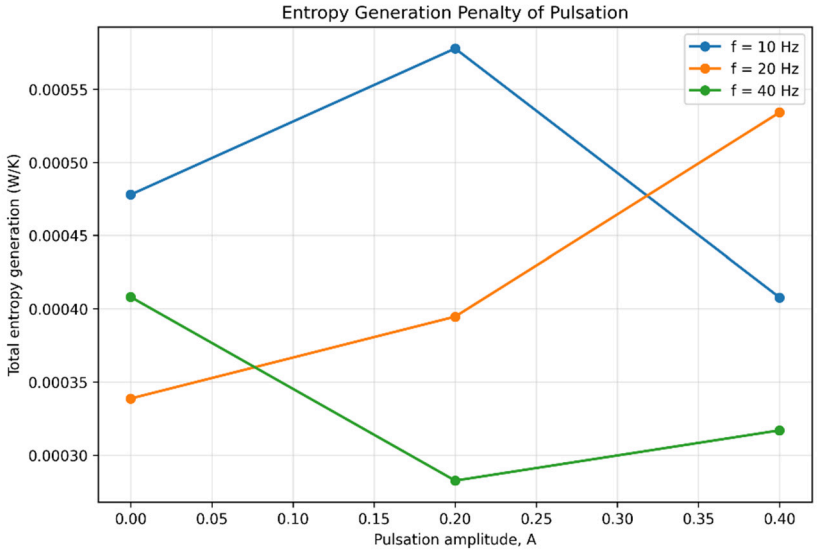


Figure 6. Variation of total entropy generation, S_{gen}, with pulsation amplitude A at f = 10, 20, and 40 Hz. The frequency-dependent and non-monotonic trends demonstrate that pulsation amplitude alone does not determine thermodynamic performance.

5.3. Spatial Distribution of Entropy Generation

The spatial distribution of entropy generation was examined to identify the regions of the channel that contribute most strongly to the overall thermodynamic irreversibility. Figure 7 presents the thermal, viscous, and total entropy-generation fields for the representative pulsating condition, allowing the integrated entropy-generation values discussed above to be related to the underlying local flow and temperature fields. The thermal entropy-generation field is concentrated mainly near the heated lower wall. This concentration is consistent with the strong temperature gradients produced by the imposed wall heat flux. Moving away from the heated surface, the thermal contribution decreases, showing that a substantial part of the thermal irreversibility is confined to the near-wall thermal region. The viscous contribution shows a different spatial pattern. It is associated with regions of strong velocity gradients and is most evident near the channel boundaries, where the no-slip condition produces significant shear. Consequently, the regions of dominant thermal and viscous irreversibility are not necessarily coincident. The total entropy-generation field represents the combined effect of these two mechanisms. Its spatial pattern is consequently influenced strongly by the thermal contribution while retaining the localized effects associated with viscous dissipation. This distinction is useful because the integrated S_{total} reported in the previous section gives the overall magnitude of irreversibility but does not indicate where that irreversibility is generated. The spatial fields also provide a physical link between the transient flow response and the entropy-generation results. Pulsation changes the instantaneous velocity and temperature distributions, and these changes modify the local velocity and temperature gradients that enter the viscous and thermal entropy-generation terms. The reported S_{total} should consequently be viewed as the integrated effect of spatially distributed thermal and viscous irreversibility, rather than as a uniform penalty applied throughout the channel.

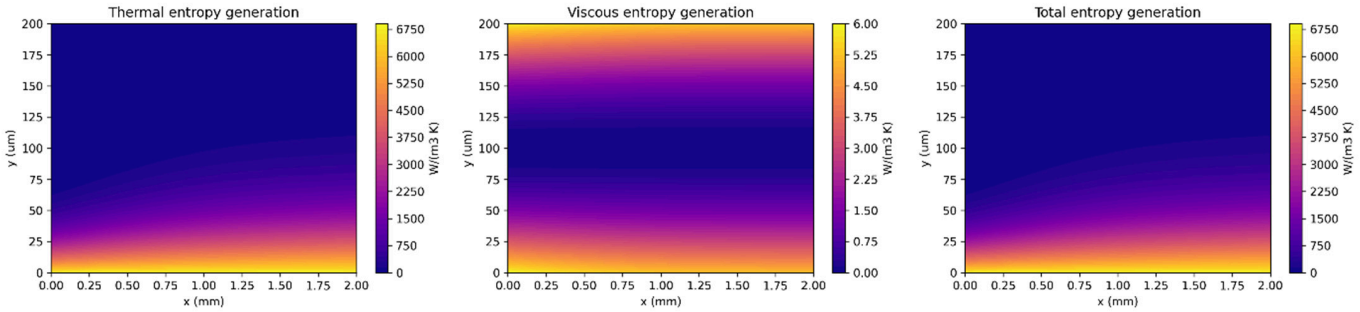


Figure 7. Spatial distribution of entropy generation for the representative pulsating condition: (**left**) thermal entropy generation, (**middle**) viscous entropy generation, and (**right**) total entropy generation. Thermal irreversibility is concentrated primarily near the heated wall, whereas viscous irreversibility is associated with regions of strong velocity gradients. The total field combines both contributions.

5.4. Parametric Summary of the Computational Study

To examine the combined effects of pulsation and nanoparticle loading, a controlled parameter sweep was performed using three pulsation amplitudes, $A = 0.0,\ 0.2$, and 0.4, three forcing frequencies, $f = 10,\ 20$, and 40 Hz, and three paired nanoparticle-volume-fraction levels. Here, ϕ_1 denotes the Al_2O_3 volume fraction and ϕ_2 denotes the Cu volume fraction. The paired concentration levels considered were $(0.005, 0.005)$, $(0.010, 0.010)$, and $(0.015, 0.015)$, giving a total of 27 computational cases. The parameter matrix follows the executable implementation. For each configuration, the transient PINN was trained, and the final trained cycle was evaluated at phase 0.50. The reported mean Nusselt number therefore represents the spatially averaged heat-transfer response at a common phase of the final pulsation cycle rather than a cycle-averaged value. The same predicted flow and temperature fields were used to calculate the integrated entropy generation, including its thermal and viscous contributions. A configuration was classified as reliable when at least 90% of the local Nusselt number values were valid and both the mean Nusselt number and total entropy generation were finite. This criterion was used only as a numerical screening rule to exclude invalid computational results from the subsequent analysis; it is not an independent validation criterion or a measure of experimental uncertainty. The complete field-level quantities, validity measures, and reliability classifications for all 27 cases are provided in Supplementary Table S4. The completed sweep shows that the heat-transfer response does not follow a simple monotonic dependence on pulsation amplitude or frequency. For example, at $f = 20$ Hz and $\phi_1 = \phi_2 = 0.015$, increasing the amplitude from $A = 0$ to $A = 0.2$ increases the mean Nusselt number from 5.5406 to 7.1126, whereas a further increase to $A = 0.4$ reduces it to 4.4215. Similar non-monotonic responses occur for other combinations of frequency and nanoparticle loading. The completed cases are therefore more appropriately interpreted as a response map over the investigated parameter space, rather than as evidence of a universal amplitude or frequency trend. The non-pulsating cases with $A = 0$ require particular care when interpreting frequency. Because the pulsation term in the inlet condition vanishes at $A = 0$, changing the nominal frequency does not introduce physical pulsation. These cases are therefore treated as separate numerical realizations of the same non-pulsating reference condition and are not interpreted as demonstrating a physical frequency effect at $A = 0$.

The combined heat-transfer and entropy-generation results were subsequently used for the Pareto analysis. Among the 27 completed cases, the condition

$$A = 0.2, f = 20 \text{ Hz}, \phi_1 = \phi_2 = 0.015$$

gives a mean Nusselt number of 7.1126 and a total entropy-generation rate of 2.7496 × 10^{-4} W/K. Within the completed parameter set, this condition is identified as the non-dominated condition, rather than as a universal optimum. The Pareto analysis is therefore restricted to the finite parameter domain examined in this study. The heat-transfer and entropy-generation responses obtained from the completed parameter sweep are summarized in Table 4.

Table 4. Compact summary of heat-transfer and entropy-generation responses for the completed parameter sweep.

A	f (Hz)	ϕ_1=ϕ_2	Mean Nu	S_{gen} (W/K)
0.0	10	0.005	7.0131	3.1515×10^{-4}
0.0	10	0.010	4.8387	4.7791×10^{-4}
0.0	10	0.015	5.2786	3.5887×10^{-4}
0.0	20	0.005	6.8075	2.7688×10^{-4}
0.0	20	0.010	6.7670	3.3868×10^{-4}
0.0	20	0.015	5.5406	3.4169×10^{-4}
0.0	40	0.005	6.1266	3.4103×10^{-4}
0.0	40	0.010	4.9585	4.0810×10^{-4}
0.0	40	0.015	6.3275	3.0931×10^{-4}
0.2	10	0.005	4.3835	5.0841×10^{-4}
0.2	10	0.010	3.9133	5.7783×10^{-4}
0.2	10	0.015	5.0948	3.9690×10^{-4}
0.2	20	0.005	6.5160	3.3341×10^{-4}
0.2	20	0.010	5.0614	3.9468×10^{-4}
0.2	**20**	**0.015**	**7.1126**	2.7496×10^{-4}
0.2	40	0.005	5.6048	3.4651×10^{-4}
0.2	40	0.010	6.3668	2.8254×10^{-4}
0.2	40	0.015	4.7728	4.3995×10^{-4}
0.4	10	0.005	5.3153	3.8182×10^{-4}
0.4	10	0.010	5.3405	4.0776×10^{-4}
0.4	10	0.015	6.3961	2.8558×10^{-4}
0.4	20	0.005	6.7563	3.3974×10^{-4}
0.4	20	0.010	4.1088	5.3413×10^{-4}
0.4	20	0.015	4.4215	4.1378×10^{-4}
0.4	40	0.005	5.0743	3.9868×10^{-4}
0.4	40	0.010	5.7640	3.1694×10^{-4}
0.4	40	0.015	4.6626	4.3252×10^{-4}

Note: A is the pulsation amplitude, f is the nominal pulsation frequency, and ϕ_1 and ϕ_2 are the Al_2O_3 and Cu volume fractions, respectively. The mean Nu is the spatially averaged Nusselt number evaluated at phase 0.50 of the final trained pulsation cycle. S_{gen} is the corresponding integrated total entropy-generation rate. The complete parametric dataset, including T_{min}, T_{max}, u_{max}, validity fraction, and reliability classification, is provided in Supplementary Table S4.

6. Heat-Transfer–Entropy Trade-Off and Pareto Optimization

The preceding results show that the response of the pulsating microchannel is governed by the combined effects of pulsation amplitude, frequency, and nanoparticle concentration. Since these parameters influence both heat transfer and thermodynamic irreversibility, evaluating a condition using the Nusselt number alone does not provide a complete assessment of its performance. Accordingly, the completed parameter sweep was evaluated using two objectives simultaneously:

$$\max Nu_{\text{mean}}$$

and

$$\min S_{\text{gen}},$$

where Nu_{mean} is the spatially averaged Nusselt number and S_{gen} is the integrated total entropy generation. In the sweep, both quantities were obtained from the same predicted thermo-fluid field at phase 0.50 of the final trained pulsation cycle. Thus, the comparison is made at a common point in the final cycle rather than using a cycle-averaged response. This two-objective formulation allows the thermal benefit of pulsation to be considered together with its thermodynamic cost.

6.1. Why a Single-Objective Optimum Is Insufficient

A higher Nusselt number represents stronger convective heat transfer, whereas a lower entropy-generation rate corresponds to lower thermodynamic irreversibility. These two quantities do not necessarily change in the same direction because variations in pulsation modify the velocity and temperature fields simultaneously.

Consequently, the relevant question is not simply which configuration produces the largest Nu_{mean}, but whether a heat-transfer improvement is accompanied by an acceptable level of entropy generation. The completed 27-case sweep was therefore analyzed using both quantities rather than selecting a condition from the heat-transfer response alone. The computational workflow explicitly stores Nu_{mean} and S_{total} for each reliable configuration before performing the Pareto analysis.

6.2. Pareto-Front Analysis

Each simulated configuration was represented by the objective pair

$$\left(Nu_{\text{mean}}\ S_{\text{gen}}\right),$$

with higher Nu_{mean} and lower S_{gen} preferred. A configuration i is considered dominated when another configuration j provides at least as large a Nusselt number and no greater entropy generation, with at least one of these inequalities being strict. The remaining configurations constitute the non-dominated set. Figure 8 presents the resulting relationship between mean Nusselt number and total entropy generation for the 27 completed cases. The Pareto analysis was performed directly on the reliable sweep data by sorting the configurations according to entropy generation and retaining the cases that progressively increase the attainable Nusselt number.

For the completed 27-case dataset, the analysis identifies a single non-dominated configuration:

$$A = 0.2, f = 20\ \text{Hz}, \phi_1 = \phi_2 = 0.015.$$

This configuration gives

$$Nu_{\text{mean}} = 7.1126$$

and

$$S_{\text{gen}} = 2.7496 \times 10^{-4}\ \text{W/K}.$$

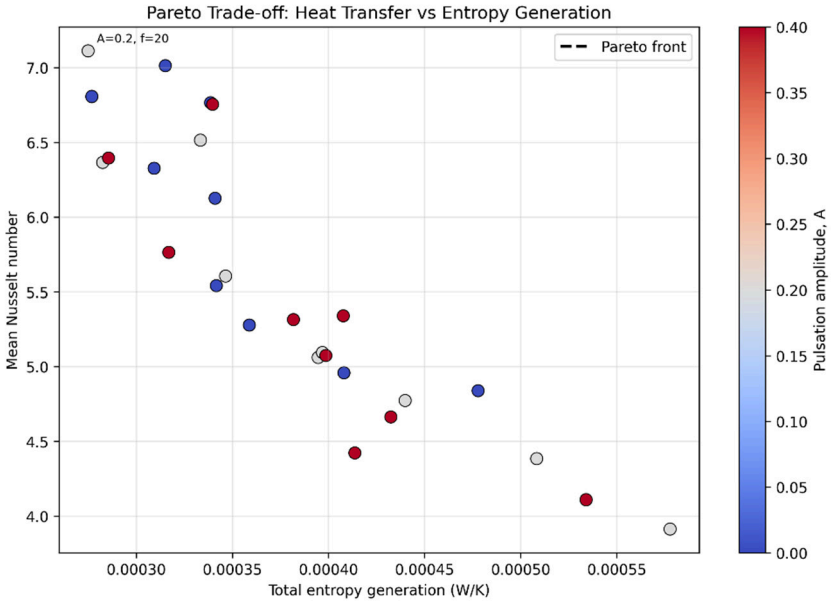


Figure 8. Pareto assessment of the completed pulsating-flow parameter sweep, showing the relationship between mean Nusselt number and total entropy generation. The Pareto front represents the non-dominated configurations under the simultaneous objectives of maximizing heat transfer and minimizing entropy generation.

The same configuration therefore provides both the highest reported mean Nusselt number and the lowest reported total entropy generation among the completed cases. The result is consistent with the implemented Pareto procedure, which identifies this point as the sole non-dominated case in the supplied 27-case dataset.

The result should, however, be interpreted within the limits of the parameter space examined. It represents a non-dominated condition within the investigated amplitude, frequency, and paired nanoparticle-concentration levels, rather than a universal optimum. A finer sweep or a wider parameter range could reveal additional non-dominated configurations and a more extended Pareto front. This limitation is particularly relevant because the present sweep contains only 27 discrete combinations.

6.3. Identification of the Preferred Operating Condition

The Pareto analysis provides a direct way to identify the operating condition that performs well with respect to both heat transfer and entropy generation. Among the 27 completed cases, the same configuration gives the highest reported mean Nusselt number and the lowest reported total entropy generation:

$$A = 0.2, f = 20 \text{ Hz}, \phi_1 = \phi_2 = 0.015.$$

For this condition,

$$Nu_{\text{mean}} = 7.1126$$

and

$$S_{\text{gen}} = 2.7496 \times 10^{-4} \text{ W/K}.$$

Thus, within the investigated parameter space, this configuration is identified as the preferred operating condition. The designation is based on the simultaneous comparison of the two calculated objectives, rather than on the Nusselt number alone. The code-based Pareto procedure identifies this case as the sole non-dominated configuration among the completed reliable cases.

6.4. Physical Interpretation

The results indicate that the influence of pulsation cannot be described by amplitude alone. The response depends on the combined effects of amplitude, frequency, and nanoparticle loading, and the resulting transient thermo-fluid field. Changes in the inlet modulation alter the velocity distribution and consequently the transport of thermal energy through the channel. The non-monotonic heat-transfer response is evident in the completed sweep. For example, at $f = 20$ Hz and $\phi_1 = \phi_2 = 0.015$, increasing the pulsation amplitude from $A = 0.2$ to $A = 0.4$ reduces the mean Nusselt number from

$$7.1126$$

to

$$4.4215.$$

Thus, a larger pulsation amplitude does not necessarily provide stronger heat transfer. The response instead depends on how the imposed pulsation interacts with the evolving thermo-fluid field.

Entropy generation also varies across the parameter space, which reinforces the need to consider both objectives together. The preferred condition produces the lowest reported value,

$$S_{\text{gen}} = 2.7496 \times 10^{-4}\ \text{W/K},$$

among the 27 completed cases. Because the sweep evaluates the final-cycle midpoint, these values describe the thermodynamic state at the common phase used for the parameter comparison rather than a full-cycle average.

The observed trends should be interpreted as model-resolved behavior within the investigated parameter range. The present results establish the relationship between the imposed operating parameters and the predicted thermo-fluid response, but they do not by themselves establish a unique microscopic mechanism responsible for every non-monotonic trend.

6.5. Engineering Significance

The main value of the Pareto analysis is that it avoids treating heat-transfer enhancement and thermodynamic irreversibility as separate performance measures. A condition that produces a high Nusselt number may not necessarily provide a favorable entropy-generation response, so selecting an operating condition from heat transfer alone can overlook this additional thermodynamic consideration.

For the 27 completed cases, the condition

$$A = 0.2, f = 20\ \text{Hz}, \phi_1 = \phi_2 = 0.015$$

is particularly notable because it simultaneously gives the highest reported

$$Nu_{\text{mean}} = 7.1126$$

and the lowest reported

$$S_{\text{gen}} = 2.7496 \times 10^{-4}\ \text{W/K}.$$

It is therefore identified as the preferred condition within the investigated parameter range. This should not be interpreted as a universal optimum, since the sweep contains only 27 discrete combinations and a broader or finer parameter space could reveal additional non-dominated solutions. The code itself performs the Pareto analysis on the completed reliable dataset rather than assuming that the identified condition is globally optimal.

More broadly, practical engineering assessment may require consideration of performance stability and long-term reliability, in addition to instantaneous thermal performance.

Recent studies in energy-conversion and advanced materials systems have similarly highlighted the importance of evaluating performance together with stability and retention under operating conditions [33,34]. Although these considerations are beyond the scope of the present transient microchannel model, they provide a broader engineering perspective for extending the present heat-transfer–entropy-generation framework toward practical design assessment.

7. Robustness, Limitations and Reproducibility

The reliability of a physics-informed neural network cannot be established from the training loss alone. A reduced loss indicates that the optimization problem has been minimized, but it does not by itself confirm the accuracy of the predicted fields or the engineering quantities derived from them. The present study therefore distinguishes between numerical verification and physical interpretation. The steady solution was compared with an independent finite-difference (FD) reference, while the transient and parametric calculations were subjected to the numerical validity checks implemented in the computational workflow. Residual-based adaptive refinement was also used to improve the resolution in regions where the governing-equation residuals remained relatively high. Together, these procedures provide a quantitative basis for assessing the computed solutions while also defining the scope within which the results should be interpreted.

7.1. Numerical Reliability

The steady PINN solution was evaluated against an independently implemented numerical benchmark that was not used during network training. The temperature profile was compared with the finite-difference (FD) solution, while the velocity profile was assessed against the analytical fully developed channel-flow reference. The resulting relative differences were 0.08% for temperature and 0.04% for velocity. For the derived heat-transfer metric, the downstream Nusselt number was 2.9969 from the PINN and 2.8953 from the FD calculation, corresponding to a relative difference of 3.51%. The somewhat larger discrepancy in the Nusselt number is expected for a derived quantity because it depends on the predicted wall temperature and temperature gradients and is therefore more sensitive to small field differences than direct profile comparisons. The parameter sweep was subsequently subjected to the numerical validity criteria implemented in the code. All completed cases reported a 100% valid fraction and were assigned a TRUE reliability flag. These checks were applied before the corresponding mean Nusselt number (Nu_{mean}) and total entropy-generation (S_{gen}) values were used in the parametric and Pareto analyses. Importantly, this reliability flag represents a numerical screening criterion, not an independent CFD or experimental validation measure. Training convergence was assessed from the evolution of the loss components together with residual-based adaptive refinement. Additional collocation points were introduced in regions identified by relatively high governing-equation residuals. Thus, solution quality was assessed using the combination of independent steady-state comparison, field-validity checks, residual behavior, and convergence history rather than by assigning significance to a single final loss value. This approach is consistent with established PINN studies that have highlighted the importance of residual balance, optimization behavior, and training-related difficulties in obtaining reliable solutions [27–30].

7.2. Limitations of the Investigated Parameter Space

The results should be interpreted as validated within a defined computational problem, rather than as universal behavior applicable to all pulsating microchannels. The present parameter study considers three amplitudes, three frequencies, and three paired nanoparticle-concentration levels, resulting in 27 completed configurations. The trends

observed within this discrete parameter space should therefore not be extrapolated beyond the investigated ranges without additional calculations. The conclusions are also specific to the channel geometry, working-fluid and effective-property models, inlet formulation, and thermal boundary conditions adopted in this study. Changes in these quantities can alter the velocity and temperature fields and, consequently, both the heat transfer and entropy generation. This is particularly relevant to the second-law analysis because entropy generation depends on the local temperature and velocity gradients and therefore responds directly to changes in the underlying thermo-fluid state [21–26].

Accordingly, the condition

$$A = 0.2, f = 20\ \text{Hz}, \phi_1 = \phi_2 = 0.015$$

should be described as the preferred condition within the investigated parameter space, rather than as a universal optimum. The transient results are likewise specific to the adopted sinusoidal pulsating inlet formulation. Other waveform shapes, frequency ranges, flow regimes, channel geometries, or boundary conditions may produce different responses. Experimental validation would therefore be required before extending the present conclusions to physical systems outside the computational configuration considered here. A further limitation is that the independent FD comparison was performed for the steady reference problem. The transient pulsating solutions were not independently benchmarked against a separate transient CFD or FD calculation for every parameter combination. The transient and parametric results should consequently be understood as extensions of the numerically verified framework rather than as individually independently validated transient solutions.

7.3. Computational Considerations of the PINN Approach

The present study does not claim that PINNs are inherently faster or computationally superior to conventional FD or CFD solvers. Transient PINN calculations can require substantial optimization because a single network must represent the spatial and temporal solution while simultaneously satisfying the continuity, momentum, and energy constraints. The value of the present approach lies instead in its integration of physics-constrained transient prediction, parameter screening, and multi-objective performance assessment within a single computational framework. After establishing the steady reference solution, the same governing formulation was extended to the transient pulsating problem and subsequently used to evaluate multiple combinations of amplitude, frequency, and nanoparticle loading. This provides a consistent route from field prediction to heat-transfer and entropy-generation analysis without claiming computational superiority over conventional numerical methods. This interpretation is consistent with the broader PINN literature, which identifies physics-informed learning as a flexible framework for forward and inverse problems while also recognizing the challenges associated with training stability and computational efficiency [27–30]. Because no controlled wall-clock or hardware-normalized comparison with a conventional CFD/FD solver was performed in the present work, no claim of computational speed-up or reduced computational cost is made.

7.4. Reproducibility and Future Extension

The computational methodology is defined through the governing equations, nondimensional variables, boundary and initial conditions, network architecture, optimization stages, precision treatment, residual-based adaptive refinement, and parameter ranges used in the calculations. The executable implementation uses a fully connected network with five hidden layers of 128 neurons, tanh activation, and the same physics-informed formulation throughout the transient calculations. The steady, baseline-transient, and parameter-sweep stages use explicitly defined optimization and collocation settings, allowing the

computational procedure to be reproduced from the reported workflow. The parameter sweep also records the configuration-specific quantities required for subsequent analysis, including Nu_{mean}, total entropy generation, thermal and viscous entropy-generation contributions, temperature limits, velocity limits, validity fraction, and the reliability flag. The complete sweep is exported by the computational workflow, while trained model checkpoints are retained for regeneration of the predicted fields. This provides a reproducible link between the trained models, derived performance metrics, and the reported Pareto analysis. The present framework can subsequently be extended to broader Reynolds number ranges, alternative channel geometries, different thermal boundary conditions, and experimental validation. Such extensions would determine whether the amplitude–frequency–nanoparticle-loading trends observed here remain consistent under different physical conditions. The multi-objective formulation can also be expanded to include quantities such as pressure drop, pumping power, maximum wall temperature, or other application-specific constraints. These additions would provide a natural progression from the present heat-transfer–entropy-generation analysis toward a more comprehensive constrained design framework.

7.5. Overall Assessment

The present study establishes a physics-informed computational framework that has been numerically verified within a clearly defined physical and numerical scope. Independent comparison of the steady reference solution gives relative differences of 0.04% for velocity, 0.08% for temperature, and 3.51% for downstream Nusselt number. All completed parameter-sweep cases also satisfy the implemented numerical validity criteria and are retained as reliable configurations for the subsequent parametric and Pareto analyses.

These results support the use of the framework for the transient and multi-objective analyses presented in this work, while the stated limitations prevent overextension of the conclusions. In particular, the identified condition,

$$A = 0.2, f = 20\ \mathrm{Hz}, \phi_1 = \phi_2 = 0.015,$$

is not presented as a universal optimum. It is the non-dominated, preferred condition within the 27-case parameter space examined here, where it simultaneously gives the highest reported mean Nusselt number and the lowest reported total entropy generation. The principal contribution is therefore the integration of physics-informed transient field prediction, independent steady-state verification, entropy-generation analysis, systematic parameter screening, and Pareto-based operating-condition selection within one workflow. This provides a more complete assessment of pulsating microchannel performance than considering heat-transfer enhancement alone, while keeping the conclusions directly tied to the numerical evidence generated by the present study.

8. Conclusions

A physics-informed neural-network framework was developed for transient pulsating microchannel flow, integrating heat-transfer and entropy-generation analysis within a common computational framework. Independent steady-state verification showed relative differences of 0.08% for the temperature profile against the finite-difference benchmark, 0.04% for the velocity profile against the analytical fully developed parabolic reference, and 3.51% for the downstream Nusselt number against the finite-difference benchmark. For the representative transient case $A = 0.30$ and $f = 20$ Hz, the Nusselt number decreased from 5.0435 to 4.5413 across the four evaluated phases, corresponding to a 9.96% decrease, while the total entropy generation increased by 11.16%. This demonstrates that the transient response is phase-dependent and that changes in heat-transfer performance are accom-

panied by changes in thermodynamic irreversibility. The completed 27-case parameter sweep showed a non-monotonic response to pulsation amplitude, frequency, and paired nanoparticle loading. Within the investigated parameter space, the condition $A = 0.2$, $f = 20$ Hz, and $\phi_1 = \phi_2 = 0.015$ was identified as the non-dominated condition, giving a mean Nusselt number of 7.1126 and a total entropy-generation rate of 2.7496×10^{-4} W/K. This result applies specifically to the tested 27-case parameter space and should not be interpreted as a universal optimum. The main contribution of the study is the integration of independent numerical verification, transient PINN modeling, systematic parameter screening, heat-transfer and entropy-generation assessment, and Pareto analysis within a single workflow. The results show that pulsation amplitude, frequency, and nanoparticle loading can interact to produce substantially different thermal responses, highlighting the need to evaluate these parameters together rather than considering heat-transfer enhancement alone. The present conclusions are limited by the finite parameter space investigated and by the absence of independent FD or CFD validation for every transient configuration. In addition, the parameter sweep represents a discrete screening of selected operating conditions rather than a continuous optimization. Future work should therefore consider finer parameter sweeps, alternative pulsation waveforms, pressure-drop and pumping-power effects, broader channel geometries and boundary conditions, and experimental validation of the transient predictions.

Supplementary Materials: The following supporting information can be downloaded at https://www.mdpi.com/article/10.3390/ijtst13020007/s1.

Funding: The authors received no specific funding for this research. The study was conducted without financial support from any public, commercial, or not-for-profit funding agency.

Data Availability Statement: The original contributions presented in this study are included in the article/Supplementary Material. Further inquiries can be directed to the author.

Acknowledgments: The author used Grammarly as a language-editing tool during manuscript preparation. Its use was limited to grammar checking, spelling correction, and language polishing. Grammarly was not used to generate, analyze, interpret, or modify the scientific results, methodology, conclusions, or technical content of the study. All scientific content, analyses, interpretations, and final decisions remain the responsibility of the authors.

Conflicts of Interest: The author declares no conflicts of interest.

References

1. Tuckerman, D.B.; Pease, R.F.W. High-performance heat sinking for VLSI. *IEEE Electron Device Lett.* **1981**, *2*, 126–129. [CrossRef]
2. Morini, G.L. Single-phase convective heat transfer in microchannels: A review of experimental results. *Int. J. Therm. Sci.* **2004**, *43*, 631–651. [CrossRef]
3. Morini, G.L. Laminar liquid flow through silicon microchannels. *J. Fluids Eng.* **2004**, *126*, 485–489. [CrossRef]
4. Kandlikar, S.G. Fundamental issues related to flow boiling in minichannels and microchannels. *Exp. Therm. Fluid Sci.* **2002**, *26*, 389–407. [CrossRef]
5. Qu, W.; Mudawar, I. Experimental and numerical study of pressure drop and heat transfer in a single-phase micro-channel heat sink. *Int. J. Heat Mass Transf.* **2002**, *45*, 2549–2565. [CrossRef]
6. Steinke, M.E.; Kandlikar, S.G. Single-phase liquid friction factors in microchannels. *Int. J. Therm. Sci.* **2006**, *45*, 1073–1083. [CrossRef]
7. Shih, T.M.; Thamire, C.; Sung, C.H.; Ren, A.L. Literature survey of numerical heat transfer (2000–2009): Part I. *Numer. Heat Transf. Part A Appl.* **2010**, *57*, 159–296. [CrossRef]
8. Mohammed, H.A.; Gunnasegaran, P.; Shuaib, N.H. The impact of various nanofluid types on triangular microchannels heat sink cooling performance. *Int. Commun. Heat Mass Transf.* **2011**, *38*, 767–773. [CrossRef]
9. Kadam, S.T.; Kumar, R. Twenty first century cooling solution: Microchannel heat sinks. *Int. J. Therm. Sci.* **2014**, *85*, 73–92. [CrossRef]

10. Coskun, T.; Cetkin, E. A review of heat and fluid flow characteristics in microchannel heat sinks. *Heat Transf.* **2020**, *49*, 4109–4133. [CrossRef]
11. Gao, J.; Hu, Z.; Yang, Q.; Liang, X.; Wu, H. Fluid flow and heat transfer in microchannel heat sinks: Modelling review and recent progress. *Therm. Sci. Eng. Prog.* **2022**, *29*, 101203. [CrossRef]
12. Yu, Z.Q.; Li, M.T.; Cao, B.Y. A comprehensive review on microchannel heat sinks for electronics cooling. *Int. J. Extrem. Manuf.* **2024**, *6*, 022005. [CrossRef]
13. Adio, S.A.; Muritala, A.O.; Binuyo, A.S.; Oketola, T.; Veeredhi, V.R. Eulerian multiphase technique for detailed investigation on hydro-thermal enhancement in a cooling microchannel using pulsating alumina nanofluid: A numerical simulation. *Case Stud. Therm. Eng.* **2024**, *59*, 104482. [CrossRef]
14. Zhou, L.; Gao, T.; Zhang, B.; Liu, D.; Gong, J.; Li, J. A comprehensive analysis of frequency and amplitude effects on pulsating flow heat transfer over a 45-degree ribbed channel. *Appl. Therm. Eng.* **2025**, *280*, 128510. [CrossRef]
15. Moon, J.W.; Kim, S.Y.; Cho, H.H. Frequency-dependent heat transfer enhancement from rectangular heated block array in a pulsating channel flow. *Int. J. Heat Mass Transf.* **2005**, *48*, 4904–4913. [CrossRef]
16. Ji, T.H.; Kim, S.Y.; Hyun, J.M. Experiments on heat transfer enhancement from a heated square cylinder in a pulsating channel flow. *Int. J. Heat Mass Transf.* **2008**, *51*, 1130–1138. [CrossRef]
17. Kim, S.Y.; Kang, B.H.; Hyun, J.M. Heat transfer in the thermally developing region of a pulsating channel flow. *Int. J. Heat Mass Transf.* **1993**, *36*, 4257–4266. [CrossRef]
18. Xu, C.; Xu, S.; Wang, Z.; Feng, D. Experimental investigation of flow and heat transfer characteristics of pulsating flows driven by wave signals in a microchannel heat sink. *Int. Commun. Heat Mass Transf.* **2021**, *125*, 105343. [CrossRef]
19. Ye, Q.; Zhang, Y.; Wei, J. A comprehensive review of pulsating flow on heat transfer enhancement. *Appl. Therm. Eng.* **2021**, *196*, 117275. [CrossRef]
20. Zamzari, F.; Mehrez, Z.; El Cafsi, A.; Belghith, A.; Le Quéré, P. Numerical investigation of entropy generation and heat transfer of pulsating flow in a horizontal channel with an open cavity. *J. Hydrodyn. Ser. B* **2017**, *29*, 632–646. [CrossRef]
21. Bejan, A. A study of entropy generation in fundamental convective heat transfer. *J. Heat Transfer* **1979**, *101*, 718–725. [CrossRef]
22. Bejan, A.; Kestin, J. Entropy generation through heat and fluid flow. *J. Appl. Mech.* **1983**, *50*, 475. [CrossRef]
23. Bejan, A. Entropy generation minimization: The new thermodynamics of finite-size devices and finite-time processes. *J. Appl. Phys.* **1996**, *79*, 1191–1218. [CrossRef]
24. Abbassi, H. Entropy generation analysis in a uniformly heated microchannel heat sink. *Energy* **2007**, *32*, 1932–1947. [CrossRef]
25. Ting, T.W.; Hung, Y.M.; Guo, N. Entropy generation of nanofluid flow with streamwise conduction in microchannels. *Energy* **2014**, *64*, 979–990. [CrossRef]
26. Samal, S.K.; Moharana, M.K. Second law analysis of recharging microchannel using entropy generation minimization method. *Int. J. Mech. Sci.* **2021**, *193*, 106174. [CrossRef]
27. Raissi, M.; Perdikaris, P.; Karniadakis, G.E. Physics-informed neural networks: A deep learning framework for solving forward and inverse problems involving nonlinear partial differential equations. *J. Comput. Phys.* **2019**, *378*, 686–707. [CrossRef]
28. Karniadakis, G.E.; Kevrekidis, I.G.; Lu, L.; Perdikaris, P.; Wang, S.; Yang, L. Physics-informed machine learning. *Nat. Rev. Phys.* **2021**, *3*, 422–440. [CrossRef]
29. Cai, S.; Mao, Z.; Wang, Z.; Yin, M.; Karniadakis, G.E. Physics-informed neural networks (PINNs) for fluid mechanics: A review. *Acta Mech. Sin.* **2021**, *37*, 1727–1738. [CrossRef]
30. Wang, S.; Teng, Y.; Perdikaris, P. Understanding and mitigating gradient flow pathologies in physics-informed neural networks. *SIAM J. Sci. Comput.* **2021**, *43*, A3055–A3081. [CrossRef]
31. Saleem, K.B.; Ismael, M.A.; Venkatadri, K.; Mir, A.; Hassen, W.; Kolsi, L.; Ghachem, K. Multiobjective optimization of natural convection and entropy generation in a porous wavy cavity with a heated star-shaped obstacle using a hybrid nanofluid. *Discov. Nano* **2026**, *21*, 240. [CrossRef] [PubMed]
32. Li, C.; Huang, J.; Hu, Y.; Li, C.; Huang, H. Numerical study of flow and heat transfer performance in a novel microchannel under pulsating flow conditions. *Int. J. Heat Fluid Flow* **2026**, *119*, 110228. [CrossRef]
33. Wu, X.; Ye, C.; Wang, Y.; Liao, Z.; Zhang, W.; Liu, W. Negative enthalpy delivering improved thermal stability for Mg2Sn-based thermoelectric power generator. *Acta Mater.* **2025**, *289*, 120865. [CrossRef]
34. Wu, X.; Mori, T.; Liu, W. Thermoelectric stability as a design constraint for energy conversion. *Joule* **2026**, *10*, 102421. [CrossRef]

Disclaimer/Publisher's Note: The statements, opinions and data contained in all publications are solely those of the individual author(s) and contributor(s) and not of MDPI and/or the editor(s). MDPI and/or the editor(s) disclaim responsibility for any injury to people or property resulting from any ideas, methods, instructions or products referred to in the content.